ELSEVIER

Contents lists available at ScienceDirect

Earth and Planetary Science Letters

journal homepage: www.elsevier.com/locate/epsl





CO₂ flushing and redox as drivers of pre-eruptive amphibole breakdown

Paul A. Wallace ^{a,*} , Sarah H. De Angelis ^b, Jessica Larsen ^c, Luca Caricchi ^d, Jackie E. Kendrick ^a , Yan Lavallée ^a

- a Department of Earth and Environmental Sciences, Ludwig-Maximilians-Universität München, Munich 80333, Germany
- ^b Tornillo Scientific, Liverpool L17 OBX, UK
- ^c Geophysical Institute, University of Alaska Fairbanks, Fairbanks AK 99775, USA
- ^d Department of Earth Sciences, University of Geneva, Geneva 1205, Switzerland

ARTICLE INFO

Editor: Dr C. M. Petrone

Keywords: Amphibole breakdown CO2 flushing Reaction rim Redox Silicic magma Volcanology

ABSTRACT

Amphibole reaction rims record critical pre-eruptive magmatic processes, including storage and ascent dynamics. Although decompression and heating are traditionally viewed as key triggers for amphibole breakdown, variations in rim textures and mineralogy indicate that multiple or fluctuating processes often operate simultaneously. This study presents experimental results demonstrating significant impacts of CO₂ flushing and redox (fO₂) conditions (versus heating and decompression) on amphibole reaction rim formation in rhyolitic and rhyodacitic melts at shallow crustal conditions. In experiments at 830 °C and 120 MPa, the presence of a mixed XH₂O:XCO₂ fluid ($XCO_2 = 0.3-0.7$) rapidly induced a reaction, with rim thickness, grain size, aspect ratio, nucleation rate and crystal number density all increasing with CO₂ concentration. In contrast, rims produced by heating (880 °C for up to 48 h) had distinct characteristics, while decompression (120 MPa to 65 MPa over 120 h) from the same starting conditions did not produce reaction rims. Increasing oxygen fugacity (fO2 from NNO+1 to RRO [NNO+2]) led to rapid rim formation within 24 h, accompanied by distinct mineralogical changes that favoured the stability of Fe³⁺ phases. These findings demonstrate that CO₂, fO₂, heating and decompression each exert unique influences on amphibole breakdown; thus, quantitative textural analysis of amphibole rims can help differentiate the driving mechanisms. Recognising the full range of factors affecting amphibole stability and an understanding of the multi-parametric controls is essential for accurately interpreting pre-eruptive conditions, enhancing our ability to reconstruct magmatic histories, and for assessing volcanic hazards.

1. Introduction

Crystal cargoes in volcanic systems serve as vital petrological records that capture the evolution of magma as it ascends from source-to-surface. These crystalline phases dynamically interact with the surrounding melt and volatiles, recording changes in magmatic conditions over time (e.g., Mollo and Hammer, 2017). Crystal disequilibrium textures, which form when the system undergoes perturbations, can provide records of changes in pressure, temperature and/or volatile content (Tepley et al., 2000; Rutherford and Devine, 2003; Cashman and Blundy, 2013; La Spina et al., 2016). Disequilibrium features manifest as zoning patterns, dissolution and resorption textures, and reaction rims at the crystal–melt interface, with their occurrence and characteristics providing crucial clues about the processes preceding and accompanying volcanic eruptions (e.g., Streck, 2008).

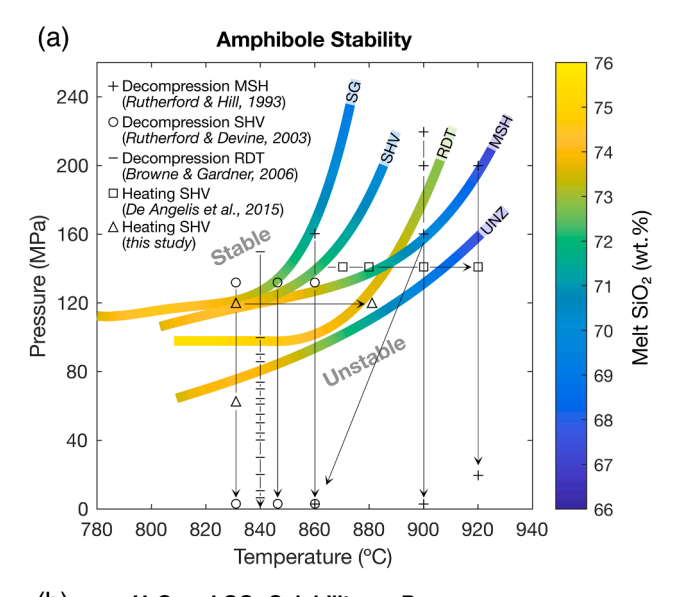
Amphibole, a prevalent hydrous mineral in intermediate to silicic

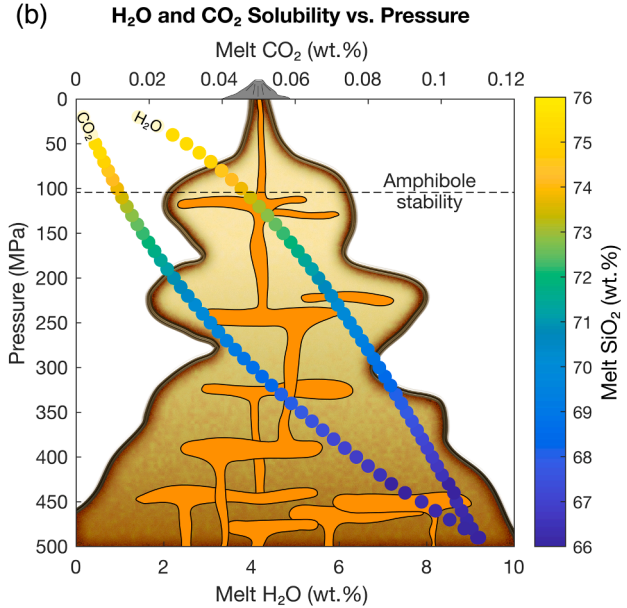
volcanic systems, is particularly sensitive to variations in pressure, temperature and chemical composition of the system (P–T–X; e.g., Ridolfi et al., 2010; Erdmann et al., 2014). When amphibole shifts outside of its stability field (Fig. 1a) it undergoes destabilisation, forming disequilibrium textures such as resorption and/or reaction rims composed of anhydrous phases that may include orthopyroxene, clinopyroxene, plagioclase and Fe-Ti oxides. As such, these textures offer a window into the changing magmatic environment (Rutherford and Hill, 1993; Browne and Gardner, 2006; Plechov et al., 2008; Kiss et al., 2014; De Angelis et al., 2015). Understanding the mechanisms behind the formation of amphibole reaction rims, with their intricate textures and diverse mineral assemblages, offers a powerful tool to unravel the timing and conditions of pre-eruptive magmatic processes, enabling more accurate interpretations of magma evolution and potential eruption triggers.

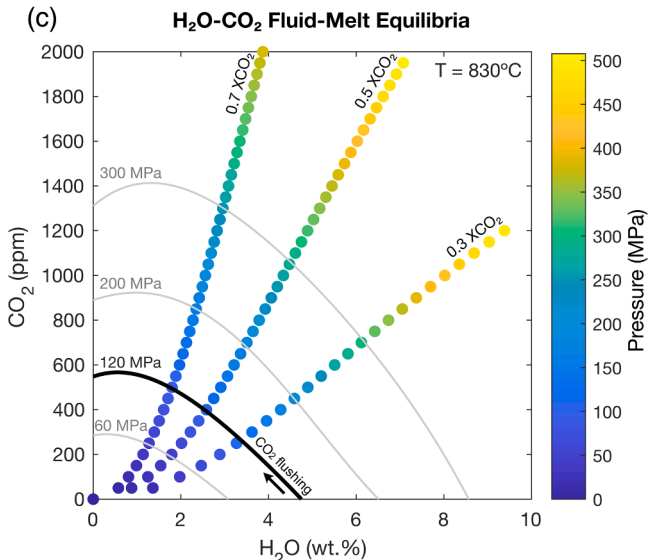
E-mail address: Paul.Wallace@min.uni-muenchen.de (P.A. Wallace).

https://doi.org/10.1016/j.epsl.2025.119532

^{*} Corresponding author.







(caption on next column)

Fig. 1. (a) Experimentally determined amphibole stability fields derived from phase equilibria studies of five well-known silicic volcanic systems: Soufrière Hills Volcano (SHV, Lesser Antilles), Mount St. Helens (MSH, Cascade Arc), Redoubt volcano (RDT, Aleutian Arc), Unzen (UNZ, Japan) and Santiaguito (SG, Guatemala). The stability curves were systematically modelled using rhyoliteMELTS thermodynamic calculations to determine the predicted equilibrium compositions of interstitial melts along the stability boundaries under varying pressure-temperature conditions. The diagram integrates data points from all previously published experimental investigations examining amphibole stability and breakdown mechanisms during both decompression and heating scenarios, with distinct symbols denoting the specific pressure-temperature conditions employed in each study. This compilation allows for direct comparison between natural systems and experimental constraints on amphibole stability fields. (b) Visualisation of rhyoliteMELTS thermodynamic modelling results illustrating the relationship between dissolved H2O and CO2 contents and pressure during isothermal fractional crystallisation at 830 °C using a starting composition representative of SHV andesitic magma. The superimposed amphibole stability curve demonstrates that under isothermal conditions of 830 °C, amphibole becomes thermodynamically unstable at pressures below 110 MPa, corresponding to conditions where the dissolved H₂O content of the melt drops below ~4 wt. % and the residual melt composition becomes increasingly evolved, exceeding 74 wt. % SiO2. This relationship highlights the critical role of melt H₂O content in controlling amphibole stability during magmatic evolution. Schematic plumbing system modified from Cashman et al. (2017). (c) H₂O-CO₂ fluid-melt equilibria in rhyolitic magmatic systems as a function of varying XCO₂ (molar fraction of CO₂ in the fluid phase). Isobars (solid lines) and fluid isopleths (dots) were calculated with VolatileCalc (Newman and Lowenstern, 2002). The diagram illustrates how systematic increases in fluid XCO₂ from 0.3 to 0.7 fundamentally alter fluid-melt equilibrium conditions by triggering enhanced H₂O exsolution from the melt phase. This process necessitates the establishment of new equilibrium dissolved volatile contents at a given pressure condition, as demonstrated by the shifting positions of isopleths. The relationship demonstrates the complex interplay between mixed volatile species controlling fluid-melt equilibria and, by extension, the stability of hydrous phases such as amphibole in evolving magmatic systems.

1.1. Current models of amphibole breakdown

Early investigations by Garcia and Jacobson (1979) laid the groundwork for understanding reaction rims by classifying them into 'black rims' and 'gabbroic' rims. The formation of 'black' rims, typically fine-grained and dominated by Fe-Ti oxides and pyroxenes, was thought to reflect high-oxygen fugacity (fO_2) environments at low pressures where amphibole undergoes dehydrogenation and reacts with surrounding melt. Conversely, 'gabbroic' rims were believed to reflect decompression as the H_2O solubility of the melt decreases, forcing the amphibole to enter a metastable state and break down.

Subsequent work established a link between the characteristics of natural amphibole reaction rims and those formed during ascent-style decompression experiments, leading to decompression initially being recognised as the primary mechanism for reaction rim formation (Rutherford and Hill, 1993; Browne and Gardner, 2006). Based on amphiboles from Mount St. Helens (USA), Rutherford and Hill (1993) experimentally demonstrated that reaction rim thickness and texture can serve as proxies for magma ascent rate, with rapid decompression leading to thin rims with acicular microlites dominated by orthopyroxene, or no breakdown at all, and slower decompression rates resulting in thicker, coarser grained rims. Browne and Gardner (2006) refined this understanding by showing that different styles of ascent (i.e., multi-step vs. single-step decompression) and final storage pressures (i.e., degree of undercooling, ΔT) resulted in different reaction rim microlite sizes and shapes in samples from Redoubt Volcano (USA). These experimental observations have been widely applied to interpret natural amphibole rims in various volcanic systems (Devine et al., 1998; McCanta et al., 2007; Scott et al., 2012; Kiss et al., 2014).

However, decompression alone cannot account for all observed reaction rims. Natural reaction rims often exhibit complex textures likely associated with different disequilibrium conditions. Experimental

studies by Rutherford and Devine (2003) and De Angelis et al. (2015) showed that heating can also play a significant role in amphibole breakdown. Heat-driven reactions lead to thicker, blocky rims with mineral assemblages that include clinopyroxene, orthopyroxene, plagioclase and Fe-Ti oxides, indicating thermal destabilisation beyond amphibole's stability field (Fig. 1a). These findings revealed that thermal input (e.g., from hotter, mafic magma injections/underplating or shear-induced heating) can trigger breakdown, producing distinct textures to those formed purely by decompression. This differentiation expanded the framework for interpreting amphibole breakdown, showcasing that multiple conditions and underlying magmatic processes can contribute to rim formation (e.g., Kiss et al., 2014; D'Mello et al., 2021).

1.2. Unexplored influence of CO₂ and fO₂ variability

Despite significant progress in understanding the role and impact of decompression and heating as mechanisms for amphibole breakdown, other factors influencing amphibole stability have been hypothesised but remain unexplored. One such factor is the impact of CO₂-bearing fluids. In magmatic systems, H2O and CO2 are the most abundant volatile components and their ratios vary across magmatic systems owing to their contrasting solubilities in silicate melts. Their presence as a dissolved and exsolved phase plays a crucial role in the physicochemical properties of magma, modulating magmatic processes (Caricchi et al., 2018; Pistone et al., 2021). Arc volcanoes are particularly important CO₂ emitters (Burton et al., 2013; Aiuppa et al., 2019). Magmas stored at shallow crustal depths often experience depletion in CO2 owing to its lower solubility compared with that of H₂O (Fig. 1b), causing preferential exsolution during decompression (Fig. 1b; Newman and Lowenstern, 2002; Ghiorso and Gualda, 2015). However, evidence suggests that CO2 can be reintroduced into shallow magmas through deep-seated magma recharge (Papale and Polacci, 1999; Newman and Lowenstern, 2002; Blundy et al., 2010) or decarbonation reactions of carbonate-hosted systems (e.g., Deegan et al., 2010; Arzilli et al., 2023). The interaction of CO₂-bearing fluids (herein termed CO₂ flushing) with shallow magmas would likely have implications for the stability of hydrous mineral phases, such as amphibole, because it impacts the volatile budget of the melt, consequently impacting the fluid-melt equilibrium by triggering moderate CO2 dissolution and excessive H2O exsolution (Fig. 1c; e.g., Newman and Lowenstern, 2002). While some studies have highlighted the effects of CO₂-bearing fluids on melt and crystal textures (e.g., Rader and Larsen, 2013; Riker et al., 2015; Giuffrida et al., 2017), the specific impact on amphibole breakdown has not been experimentally quantified.

Another important variable that could influence amphibole breakdown is fO2, a measure of the availability or potential of oxygen in a magmatic system; in other words, fO2, represents the partial pressure of oxygen that would be in equilibrium with the magma at a given temperature, pressure and composition (Carmichael and Ghiorso, 1990). The fO_2 of a magmatic system is influenced by various factors, including the source region composition, degree of partial melting, extent of magma differentiation, chemistry of dissolved and exsolved volatiles, and interaction with crustal rocks (e.g., Carmichael, 1991; Frost and McCammon, 2008; Sun and Lee, 2022). Even within a single volcanic system it can vary by up to several orders of magnitude during crystallisation (Kolzenburg et al., 2018). The redox state of a magma, commonly expressed in terms of fO_2 , plays a crucial role in defining the crystallisation sequence, stability of ferromagnesian phases, degassing behaviour of volatiles and physical properties of magmas (Dingwell and Virgo, 1987; Scaillet et al., 1998; Kolzenburg et al., 2018; Tollan and Hermann, 2019; Hughes et al., 2024). Despite this, most experimental studies on amphibole breakdown have been conducted at fixed fO2 conditions, typically near the nickel-nickel oxide (NNO+1) buffer (Rutherford and Hill, 1993; Rutherford and Devine, 2003; Browne and Gardner, 2006). This limited experimental focus restricts understanding of how variations in redox conditions influence amphibole reaction rim formation.

1.3. Complexity of natural systems

In natural volcanic systems, amphibole reaction rims often display complex, multifaceted textures that suggest multiple destabilising controls acting simultaneously or sequentially. These textures can be challenging to interpret, and owing to the limited scope of experimental work to date, there is an overwhelming bias in the literature towards either heating or decompression. Detailed studies of amphibole rims from various volcanoes, including Soufrière Hills Volcano (Montserrat; Devine et al., 1998; Rutherford and Devine, 2003; Buckley et al., 2006), Mount St. Helens (USA; Rutherford and Hill, 1993) and Ciomadul Volcano (Romania; Kiss et al., 2014) have revealed mineralogical and textural variability pointing to multi-mechanism, multi-stage processes, challenging the adequacy of single-mechanism interpretations. Given the complex and interacting nature of these influences, interpretations based solely on decompression or heating inevitably involve some degree of oversimplification.

This study aims to integrate CO_2 flushing and fO_2 variability into the current dichotomous amphibole breakdown model (i.e., decompression or heating), expanding the experimental framework to enable more accurate reconstructions of natural magmatic systems. The implications of these findings extend beyond proof of concept, as they can contribute to broader assessments of magmatic conditions by offering new insights into magma-fluid interaction during transport that influences eruption styles.

2. Materials & methods

To investigate the effects of CO_2 flushing, $f\mathrm{O}_2$, heating and decompression on amphibole breakdown and reaction rim formation, we designed a series of controlled experiments to simulate natural magmatic conditions and systematically isolate the influences of each variable on amphibole stability.

2.1. Starting materials

We conducted experiments using three sets of starting materials (Table 1): (1) Amphibole-seeded rhyolite at $fO_2 = \text{NNO}+1$; (2) Amphibole-seeded rhyodacite at $fO_2 = \text{NNO}+1$; (3) Amphibole-seeded rhyolite at $fO_2 = \text{Re}-\text{ReO}$ (RRO). For sets (1) and (2), we added a XH₂O:XCO₂ fluid with molar ratios of 0, 0.3, 0.5 and 0.7 XCO₂, with or without a heating or decompression step. Set (3) was performed with a pure H₂O fluid phase. These conditions span the range of fluid compositions found in natural volcanic systems.

All starting materials were crystal-poor, with rhyolite from Panum Crater, California (Mangan and Sisson, 2000; Burgisser, 2003) and the rhyodacite from Aniakchak Volcano, Alaska (Larsen, 2006). These compositions span the typical range for natural high-silica melts found in evolved, amphibole-bearing magmatic systems. Each were ground to fine powders to ensure homogeneity. Magnesio-hornblende amphibole crystals were manually separated from an andesitic block with a rhyolitic interstitial glass erupted from Soufrière Hills Volcano, Montserrat (Fig. 2a; De Angelis et al., 2015). Amphibole grains were lightly crushed, cleaned in a 63- μ m sieve, and hand-picked under a binocular microscope to ensure size and purity. In each experiment, ~5 wt. % amphibole was mixed with ~0.05 g of glass powder to simulate natural amphibole–melt interactions.

Phase equilibria experiments and thermodynamic models (Fig. 1b) indicate that at typical shallow magma storage conditions (830 °C, 120 MPa/~5 km depth), close to amphibole's lower stability limit, the interstitial melt composition is rhyolitic–rhyodacitic (Fig. 1b; Barclay et al., 1998; Rutherford and Devine, 2003; Andrews, 2014). At these conditions, previous work has shown that the melt and amphiboles are

 Table 1

 Experimental conditions and mean reaction rim measurements.

Experimental setup					Average (std. dev.) reaction rim measurements ($n=\geq 4$ rims per experiment)					
Exp.*	XCO ₂	fO ₂	Initial conditions <i>T/P/t</i>	Second conditions <i>T/P/t</i>	Width μm	Grain size μm	Aspect ratio	[†] Na mm ⁻²	§I mm⁻³ s⁻¹	#G mm s ⁻¹
RL_1	0.0	NNO+1	830/120/24	_	n/a	n/a	n/a	n/a	n/a	n/a
RL_3_2	0.3	NNO+1	830/120/24	_	5 (2)	2(1)	3 (2)	$6.1(4.5)\times10^3$	33.2	1×10^{-7}
RL_3_3	0.5	NNO+1	830/120/24	_	9 (6)	5 (4)	9 (6)	$2.3(1.7)\times10^4$	55.4	$5 imes 10^{-8}$
RL_3_4	0.7	NNO+1	830/120/24	_	8 (7)	5 (4)	13 (7)	$3.0(3.1)\times10^4$	64.0	$5 imes 10^{-8}$
RL_4	0.3	NNO+1	830/120/24	880/120/24	10 (6)	7 (4)	2(2)	$4.1(3.5)\times10^3$	3.5	7×10^{-8}
RL_2	0.0	NNO+1	830/120/24	880/120/24	n/a	n/a	n/a	n/a	n/a	n/a
RL_2_2	0.0	NNO+1	830/120/24	880/120/48	25 (10)	15 (9)	3 (2)	$1.5(2.5)\times10^{2}$	0.1	3×10^{-7}
RL_7	0.0	NNO+1	830/120/24	830/65/120	n/a	n/a	n/a	n/a	n/a	n/a
RD_2	0.0	NNO+1	830/120/24	880/120/48	n/a	n/a	n/a	n/a	n/a	n/a
RD_3	0.3	NNO+1	830/120/24	_	3 (2)	3 (3)	3 (2)	_	_	_
RD_3_2	0.5	NNO+1	830/120/24	_	4(2)	2(1)	4 (2)	_	_	_
RD_3_3	0.7	NNO+1	830/120/24	_	3(1)	1(1)	3 (1)	_	_	_
RD_11	0.0	NNO+1	830/120/24	830/65/120	n/a	n/a	n/a	n/a	n/a	n/a
RL_5	0.0	RRO	830/120/24	_	6 (1)	3(1)	7 (5)	_	_	_
RL_6	0.0	RRO	830/120/24	880/120/24	10 (8)	11 (8)	7 (6)	_	_	_

Notes:

in equilibrium and the amphibole remains stable (e.g., Rutherford and Devine, 2003), forming perfect starting conditions to constrain P–T–X controls on reaction rim formation. Full compositions of the starting materials are provided in the Electronic Supplementary Materials.

2.2. Experimental methods

Each experimental charge was loaded into a 5 mm Ag capsule (Fig. 2b). Experiments with $XH_2O = 1$ were loaded with ~ 15 wt. % deionised H2O to ensure vapour saturation. For experiments conducted with fluid compositions of $XH_2O < 1$ on a molar basis (i.e., $XCO_2 =$ 0.3–0.7), CO₂ was added by proportionally mixing (by weight) Ag₂CO₃ powder with H₂O to achieve the desired XCO₂, following the method of Rader and Larsen (2013). For NNO+1 runs, capsules were placed in cold-seal pressure vessels with Ni rods to buffer fO2 near the nickel--nickel oxide (NNO+1) level (Eugster, 1957). For RRO (∼NNO+2) runs, a double-capsule method was used: an Ag₇₀Pd₃₀ capsule with a 1:1 molar mixture of rhenium and rhenium oxide was added to the main Ag capsule. All capsules were sealed with a Puk 3 precision arc welder. Capsules were then loaded into externally heated Waspaloy® cold-seal vessels and placed in a horizontal tube furnace (Fig. 2c). Prior to experiments, temperature calibrations were performed along the length of the tube furnace using K-type thermocouples to identify and correct for any temperature offsets at the capsule position. The Waspaloy® autoclaves include an internal thermocouple well that positions a K-type thermocouple in close proximity to the sample capsule, allowing accurate monitoring of run temperatures throughout each experiment.

Pressure–temperature conditions (Table 1) were chosen to approximate shallow crustal magmatic environments. A 24 h baseline experiment (rhyolite set 1) at 830 °C, 120 MPa, NNO+1 and $XH_2O=1$ confirmed amphibole stability, consistent with known phase equilibria for several well-known silicic volcanic systems (Fig. 1a), including Soufrière Hills Volcano (Barclay et al., 1998; Rutherford and Devine, 2003), Santa Maria/Santiaguito (Andrews, 2014) and Mount St. Helens (Rutherford et al., 1985). We then performed 24 h isobaric–isothermal experiments at 830 °C and 120 MPa to test the effect of adding a mixed $XH_2O:XCO_2$ fluid (using set 1 and 2) or changing fO_2 (NNO+1 vs. RRO using set 3) on amphibole stability (Fig. 2d). For heating experiments, samples were first equilibrated at 830 °C/120 MPa for 24 h, then heated to 880 °C for an additional 24 or 48 h at $XH_2O=1$ or 0.7. Finally, a

single-step decompression experiment was conducted for both rhyolite and rhyodacite compositions: samples were held at 830 °C/120 MPa for 24 h, decompressed to 65 MPa in one step, and held for 120 h (5 days). These decompression conditions follow Browne and Gardner (2006), who showed that a single-step decompression to 65 MPa promotes reaction rim growth over several days.

Each experiment was rapidly quenched (<1 min) using compressed air, followed by water immersion, to preserve textural and mineralogical features. Capsules were weighed before and after welding and again after quenching; experiments showing any mass loss were discarded and repeated. The charges were then extracted, mounted in resin, polished, and carbon-coated for compositional and textural analyses.

2.3. Analytical methods

2.3.1. Image acquisition and textural quantification

Backscatter electron (BSE) images of amphibole reaction rims were acquired on a Hitachi TM3000 SEM (15 kV, 10 mm working distance) at the University of Liverpool. We selected 4–7 rimmed magnesio-hornblende crystals per experiment and used ImageJ (Schneider et al., 2012) to measure rim width (11–34 equally spaced measurements from the amphibole edge to the rim edge), grain size and aspect ratio (Feret's length of $\geq\!10$ representative grains), and orientation (each of amphibole's long axis normalised to one of the $60^\circ/120^\circ$ cleavage planes). When microlites formed along these cleavage planes, rose diagrams show two orientation peaks (e.g., 0–180° and $\sim\!60$ –240°), although only one plane was used as the reference if both were visible.

Crystal number density (Na) was determined by counting crystals in 2–5 regions of interest (ROI) around the rim (following De Angelis et al., 2013), and area fraction (Φ) was obtained by grid-based point counting in the same ROI. Finally, nucleation (I) and growth (G) rates were calculated following Brugger and Hammer (2010).

2.3.2. Electron probe microanalysis

Major-element compositions of glass, amphibole and reaction rim microlites were measured on a JEOL 8200 superprobe at the University of Geneva, with five WDS and one EDS. For amphibole, a \sim 5 μ m, 15 keV/15 nA focused beam was used (10–30 s on peak; 5–15 s on background). For glass, a \sim 10 μ m, 15 keV/6 nA defocused beam was used (20–30 s on peak; 10–15 s on background). For full compositions,

 $^{^*}$ All experiments initially held at T=830 °C and P=120 MPa for t=24 h. Heating experiments subsequently heated to T=880 °C for t=24 or 48 h. Decompression experiments subsequently underwent single-step decompression to P=65 MPa for 120 h.

 $^{^{\}dagger}Na = \text{crystal number density.}$

 $^{{}^{\}S}I$ = nucleation rate.

 $^{^{\#}}G = \text{growth rate.}$

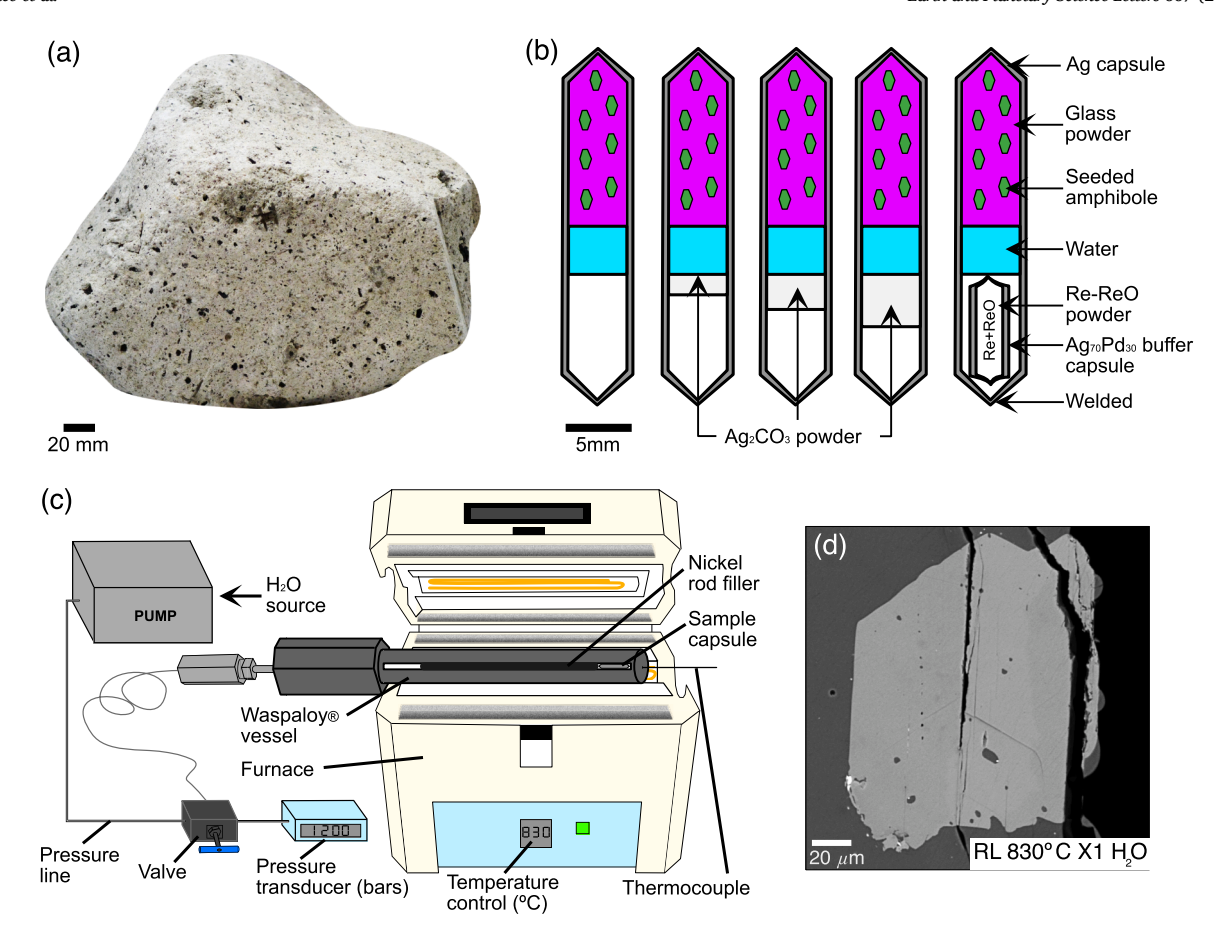


Fig. 2. Experimental apparatus and methodology. (a) Andesitic block from Soufrière Hills Volcano used for the manual extraction of amphibole crystals used for experiments. (b) Experimental capsule configurations showing the systematic loading of silver (Ag) capsules with either rhyolitic glass (Panum Crater) or rhyodacitic glass (Aniakchak), each seeded with amphibole crystals from Soufrière Hills Volcano andesite. All capsules contained sufficient H_2O (i.e., >5 wt. %) to ensure saturation at 120 MPa, with some experiments including Ag_2CO_3 powder to achieve variable $XH_2O:XCO_2$ molar ratios in the fluid phase. Additional experiments targeting more oxidising conditions utilised an $Ag_{70}Pd_{30}$ capsule (crimped only) containing rhenium–rhenium oxide (RRO) powder. All capsules were precision-welded to maintain closed-system conditions throughout the experiments. (c) Schematic illustration of the horizontal cold-seal pressure vessel and autoclave system used in this study. The experimental assembly uses water as the pressure-transmitting medium within a Waspaloy® vessel. (d) Backscatter electron (BSE) image of the baseline experiment conducted at 830 °C, 120 MPa, NNO+1 and $XH_2O = 1$ in a rhyolitic (RL) melt confirmed amphibole stability under baseline conditions, establishing control parameters for subsequent experimental variations.

methods and analytical precision and accuracy, see the Electronic Supplementary Materials.

Reaction rim microlites were analysed on a Cameca SX100 EPMA at Ludwig-Maximilians-Universität in Munich, with a 15 keV, 40 nA, $\sim \! 1$ μm focused beam. As many microlites were small and acicular ($< \! 10 \, \mu m$), only the largest were measured for accuracy. To better characterise rim mineralogy, EDS mapping was performed on a scanning electron microscope at 15 keV with scan times of 20–30 min. These maps were collected for a subset of experiments to illustrate mineralogical differences under various experimental conditions.

3. Results

The rhyolite baseline experiment (830 °C/120 MPa/NNO+1/XH $_2$ O = 1 for 24 h) produced no observable reaction rims around amphibole crystals (Fig. 2d), confirming amphibole stability under these conditions and establishing a reference point for subsequent experiments.

3.1. Effects of CO₂ concentration on reaction rim formation

Introducing CO₂ into the system (varying XH₂O:XCO₂) caused marked changes in amphibole reaction rim development at 830 °C, 120 MPa and NNO+1 for $<\!24$ h. Additionally, groundmass microlite crystallisation increased proportionally with XCO₂ in all CO₂-bearing

experiments.

3.1.1. Rhyolite melt, $XCO_2 = 0.3$ (low CO_2)

At XCO $_2=0.3$, thin rims (up to 5 µm) formed around amphiboles, composed mainly of clinopyroxene microlites with minor Fe-Ti oxides but no orthopyroxene (Fig. 3a). Microlites (<5 µm) are elongated and tabular, with aspect ratios up to 8 (Fig. 3b). Crystal number densities range from $\sim\!440$ to 10,670 mm $^{-2}$. Microlites are strongly aligned with one amphibole cleavage plane, and where amphiboles were cut perpendicular to the c-axis, microlites are generally more equant, indicating preferential alignment parallel to the c-axis.

3.1.2. Rhyolite melt, $XCO_2 = 0.5$ (moderate CO_2)

At XCO $_2$ = 0.5, rims thickened up to 19 μ m (Fig. 3c); microlites reached 23 μ m and are acicular, with aspect ratios up to 32 (Fig. 3d). Clinopyroxene dominates with minor Fe-Ti oxides. *N*a increased markedly to 41,980 mm 2 , reflecting higher nucleation and growth rates. Microlites remain strongly oriented along the amphibole cleavage planes, forming a denser texture.

3.1.3. Rhyolite melt, $XCO_2 = 0.7$ (high CO_2)

At $XCO_2=0.7$, rims reached 17 μ m (Fig. 3e), and microlites grew to 19 μ m (Fig. 3f) with aspect ratios up to 26. Mineral assemblages are similar to that in the lower-CO₂ runs. Despite similarities to $XCO_2=0.5$

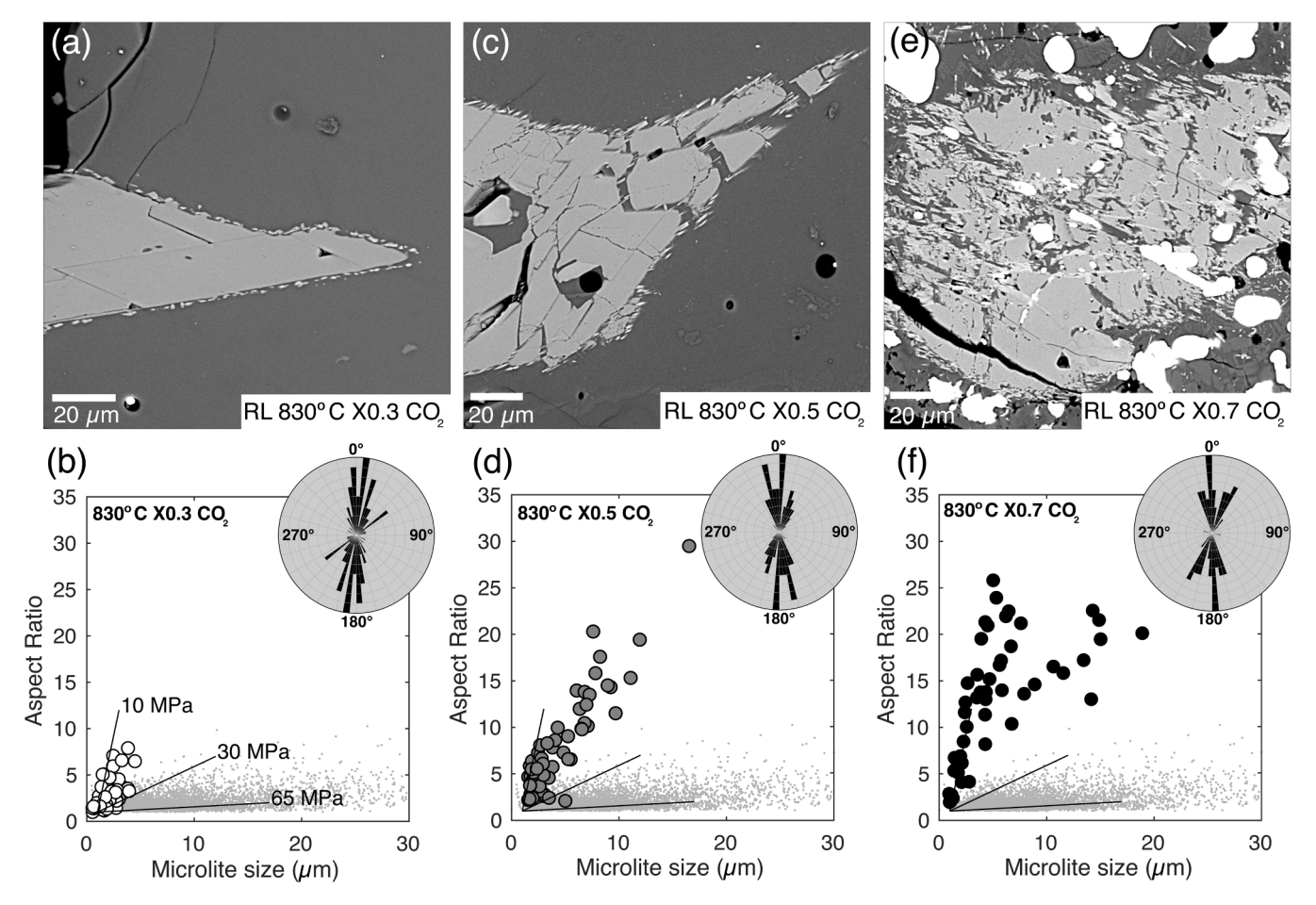


Fig. 3. Textural and quantitative analysis of experimental amphibole breakdown in a rhyolite melt as a response to CO_2 . (a, c, e) Backscatter electron (BSE) images show the systematic evolution of amphibole reaction rim textures developed under constant temperature-pressure conditions (830 °C, 120 MPa, NNO+1) but varying fluid phase compositions ($XCO_2 = 0.3, 0.5$ and 0.7). BSE images reveal distinctive systematic changes in reaction rims as a function of increasing CO_2 content. (b, d, f) Corresponding quantitative analysis of reaction rim microlites, highlighting the relationship between microlite size and aspect ratio for each XCO_2 condition. Inset rose diagrams quantify the preferential orientation of reaction products relative to visible amphibole crystallographic axis planes. These results are contextualised through comparison with previously published textural data from heating-induced breakdown experiments (light grey dots; De Angelis et al., 2015) and decompression studies conducted at various final pressures (grey lines; 10, 30 and 65 MPa; Browne and Gardner, 2006), enabling direct comparison between different mechanisms of amphibole destabilisation.

runs, *N*a rose further to 71,610 mm⁻². A strong microlite orientation persists, reflecting a pronounced response to higher CO₂.

3.1.4. Rhyodacite melt, $XCO_2 = 0.3-0.7$

Shifting to rhyodacite altered reaction rim textures (Fig. 4a–F). Microlites generally did not exceed 5 μm , except for occasional grains ($\sim\!15~\mu m$) at XCO $_2=0.3$. Their aspect ratios rarely surpass 10, although strong preferential orientations persist. Groundmass crystallisation increased systematically with CO $_2$ concentration, exceeding that observed in rhyolite runs.

3.2. Effect of heating

3.2.1. Rhyolite heating at 880 °C for 24 h

No reaction rims formed after 24 h at 880 °C (Fig. 5a,b), indicating that short-term heating at 120 MPa without added CO_2 does not induce amphibole reaction rim formation. However, amphibole edges are curved rather than straight as in baseline experiments, suggesting minor resorption.

3.2.2. Rhyolite heating at 880 °C for 48 h

Extending heating to 48 h at 880 $^{\circ}$ C produced substantial rims, up to \sim 40 μ m thick (Fig. 5c). These rims contain large, blocky microlites up to

50 μm in size, with aspect ratios <5 (Fig. 5d) and a moderate two-direction orientation (\sim 60° and 120°, offset by \sim 15° from the normalised 0° direction). Crystal number densities are relatively low (<300 mm⁻²). Some microlites are zoned core-to-rim (Fig. S1a), reflecting evolving syn-breakdown conditions. The rim assemblage include orthopyroxene, clinopyroxene and minor Fe-Ti oxides, contrasting with the clinopyroxene-dominated rims from CO₂-flushed experiments.

3.2.3. Rhyodacite heating at 880 °C for 48 h

Rims did not form on amphibole in rhyodacite melt following 48 h at 880 $^{\circ}$ C; amphibole remained stable, and the conditions even promoted new amphibole overgrowth at the amphibole–melt interface (Fig. S1b).

3.2.4. Rhyolite combined $XCO_2 = 0.3$ and heating at 880 $^{\circ}C$

Combining XCO $_2=0.3$ and heating to 880 °C produced rims with features intermediate between CO $_2$ -only and heating-only experiments (Fig. 5e). Rims average 9 μ m thickness and contain both fine and blocky microlites up to 21 μ m, with aspect ratios <5 (Fig. 5f). Microlites are strongly oriented but less so than in CO $_2$ -only runs. The rims contain orthopyroxene, clinopyroxene and minor Fe-Ti oxides, revealing dual influences from both thermal and CO $_2$ -flushing processes.

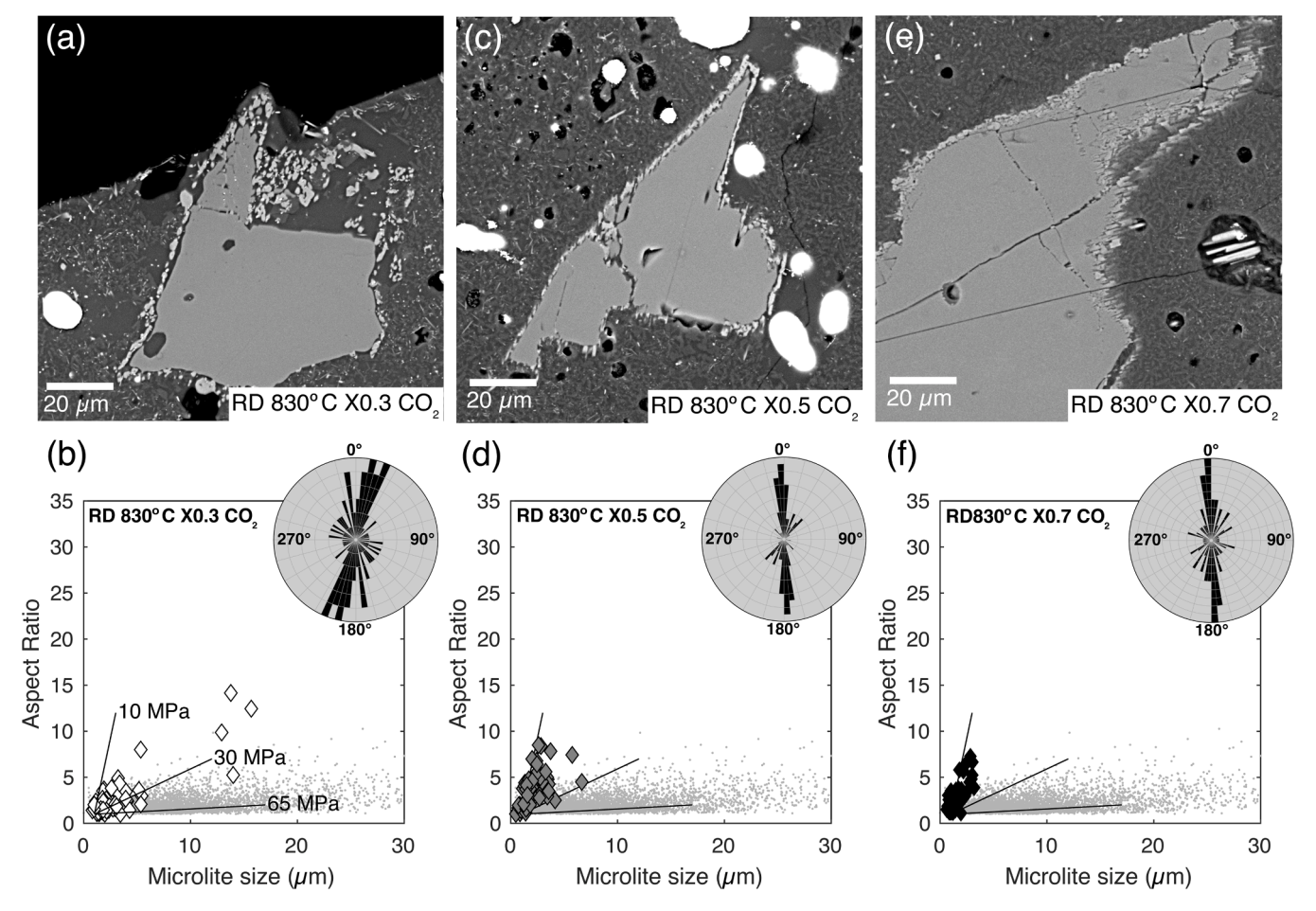


Fig. 4. Textural and quantitative analysis of experimental amphibole breakdown in a rhyodacite melt as a response to CO_2 . (a, c, e) Backscatter electron (BSE) images show the systematic evolution of amphibole reaction rim textures developed under constant temperature-pressure conditions but varying fluid phase compositions ($XCO_2 = 0.3$, 0.5 and 0.7). (b, d, f) Corresponding quantitative analysis of reaction rim microlites, highlighting the relationship between microlite size and aspect ratio for each XCO_2 condition. Inset rose diagrams quantify the preferential orientation of reaction products relative to visible amphibole crystallographic axis planes. These results are contextualised through comparison with previously published textural data from heating-induced breakdown experiments (light grey dots; De Angelis et al., 2015) and decompression studies conducted at various final pressures (grey lines; 10, 30 and 65 MPa; Browne and Gardner, 2006).

3.3. Effects of fO2 in a rhyolite melt

3.3.1. Increased fO₂ conditions (RRO)

At NNO+1 (830 °C, 120 MPa, XH $_2$ O = 1), amphibole remains stable with no reaction rims (Fig. 2d). However, at more oxidising conditions (NNO+2, or RRO), thin reaction rims (up to 6 μ m) formed (Fig. 6a). Unlike NNO+1 experiments, these rims are dominated by biotite with additional Fe-Ti oxides and plagioclase and only minor orthopyroxene. Biotite microlites (<6 μ m) display acciular morphologies (aspect ratios up to 20) with minimal preferential orientation compared with CO $_2$ - and heating-induced rims (Fig. 6b).

3.3.2. Combined heating and fO2

More oxidising conditions (RRO; $XH_2O=1$) combined with additional heating for 24 h at 880 °C produced reaction rims up to 19 μ m containing large, randomly oriented biotite microlites up to 30 μ m (Fig. 6c,d). Despite their high aspect ratios (up to 20), these microlites display lower ratios at a given size than those in non-heated RRO experiments, mirroring the effect of heating under other conditions. Overall, these rims differ from purely fO_2 -driven ones, indicating that combined heating and higher fO_2 produced intermediate textures, with fO_2 exerting a strong mineralogical control and heating having a dominantly textural control.

3.4. Decompression experiments

Two decompression experiments (from 120 MPa to 65 MPa at 830 $^{\circ}\text{C}$ and NNO+1/XH₂O = 1) were conducted with rhyolite and rhyodacite powders, but neither produced clear amphibole reaction rims after 5 days (120 h) at final pressure. In the rhyolite experiment, amphibole edges show subhedral-rounded morphologies (Fig. 6e), indicating partial resorption. In the rhyodacite, amphiboles remain euhedral, suggesting an absence of (or minimal) reaction with the melt (Fig. 6f). The absence of decompression-induced rims contrasts sharply with the rims observed in heating, CO₂ and fO₂ experiments, implying that at 830 $^{\circ}\text{C}$ decompression from 120 to 65 MPa alone may not sufficiently destabilise amphibole under the given timescale.

3.5. Effect of experimental conditions on melt and pyroxene composition

3.5.1. Melt composition

All experiments starting with Panum Crater rhyolite (76.1 wt. % SiO₂) produced melt compositions ranging from 75.7 to 78.1 wt. % SiO₂ (Fig. 8a). The baseline experiment (830 °C, 120 MPa, NNO+1, XH₂O = 1) yielded a narrow range of 77.1–77.8 wt. % SiO₂. When the temperature was raised to 880 °C for 24 h, the melt composition varied from 76.9 to 77.5 wt. % SiO₂, whereas extending the heating period to 48 h shifted the melt to 76.1–77.0 wt. % SiO₂. In CO₂-flushing experiments (XCO₂ = 0.3–0.7), the SiO₂ content of 76.5–77.9 wt. % was similar to

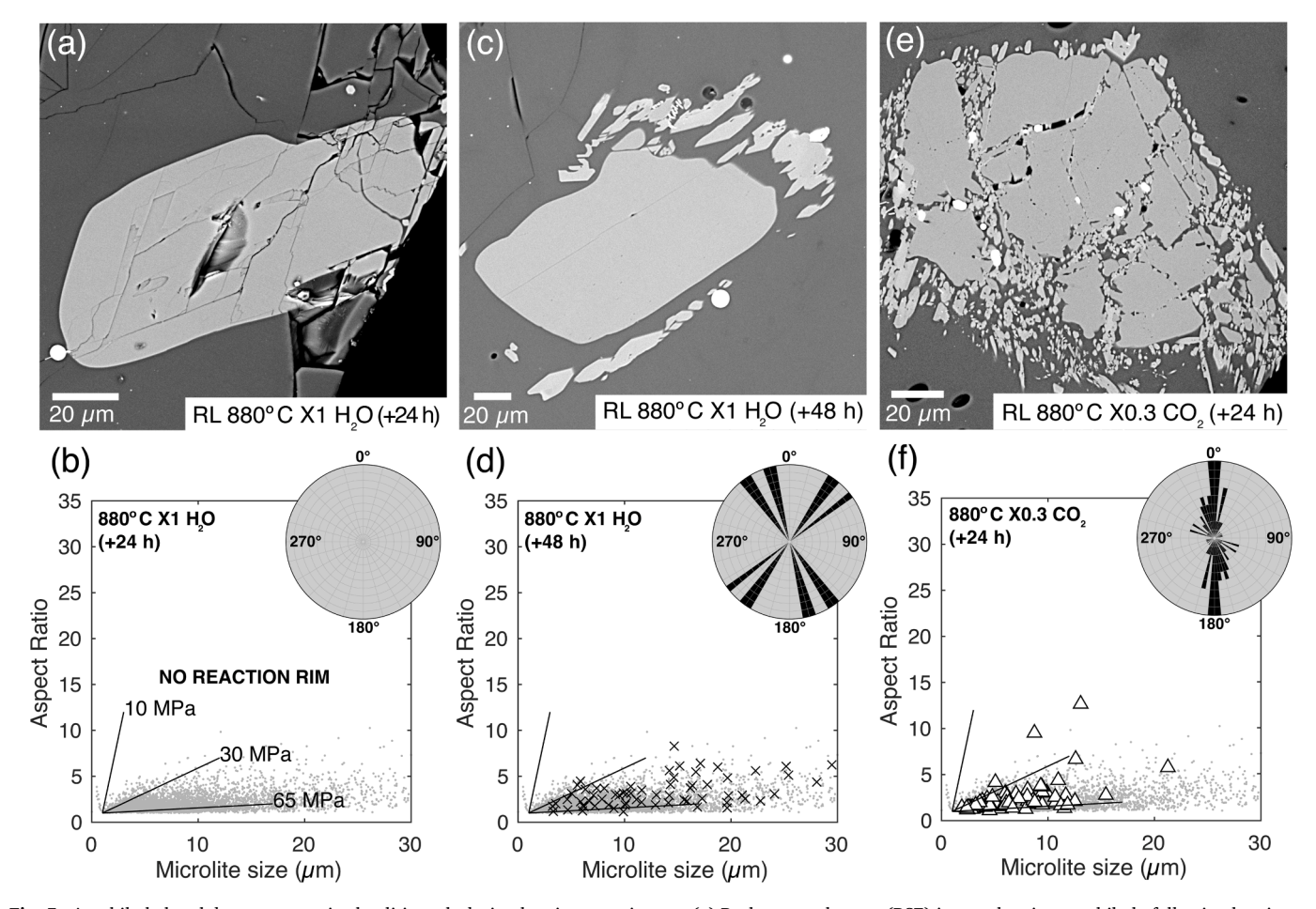


Fig. 5. Amphibole breakdown textures in rhyolitic melt during heating experiments. (a) Backscatter electron (BSE) image showing amphibole following heating to 880 $^{\circ}$ C, exhibiting curved crystal edges without reaction rims (b). (c) BSE image of amphibole after 48 h at 880 $^{\circ}$ C showing thermally-induced reaction rims characterised by the development of coarse-grained, well-formed microlites surrounding remnant amphibole cores. Note the zoned pyroxene microlite at the bottom-left of the BSE image. (d) Textural analysis of reaction rim microlites showing microlite size against aspect ratio, demonstrating textural characteristics consistent with previous thermal breakdown experiments (light grey dots; De Angelis et al., 2015). Grey lines previously published textural data from decompression studies conducted at various final pressures (10, 30 and 65 MPa; Browne and Gardner, 2006). Inset rose diagrams quantify the preferential orientation of reaction products relative to visible amphibole crystallographic axis planes. (e) Multi-variable experiment showing the combined influence of elevated temperature (880 $^{\circ}$ C) and mixed volatile conditions (XCO₂ = 0.3) after 24 h, with corresponding quantitative textural analysis of reaction products presented in (f).

that of the baseline but showed a broader compositional range. Glass composition for the $XCO_2 = 0.7$ experiments showed subtle effects of microlite crystallisation, particularly evident in the elevated K2O contents (Fig. S2). Combining heating with CO2 led to compositions with lower SiO₂ (75.7–77.1 wt. %), reflecting the influence of both processes. Under more oxidised conditions (RRO), melt compositions clustered within 77.6-78.0 wt. % SiO₂, whereas the combination of elevated fO₂ and heating shifted this range to 77.0-77.8 wt. % SiO2 (Fig. 8a). Variations in FeO total concentrations proved particularly noteworthy across experimental conditions. Relative to the Panum Crater rhyolite (1.0 wt. % FeO_t) and baseline experiment (1.0–1.2 wt. % FeO_t), experiments that involved an additional heating stage showed elevated FeOt content (1.2-1.6 wt. %), except when combined with increased fO2. Melts at RRO contained the lowest FeO_t concentrations (0.8–1.0 wt. %), though these values increased slightly when combined with heating (1.0-1.2 wt. % FeOt). Variations in CaO and MgO followed broadly similar patterns to FeOt (Fig. S2).

Experiments using Aniakchak rhyodacite (70.6 wt. % SiO_2) yielded melts enriched by approximately 6 wt. % SiO_2 compared with the starting material (Fig. 8a). Because of extensive microlite crystallisation, glass analyses were only possible in runs with sufficient interstitial melt. Heating produced more evolved compositions of 72.1–72.8 wt. % SiO_2 , whereas CO_2 flushing increased SiO_2 to 75.8–76.4 wt. %, yielding values

comparable to those seen in the rhyolite experiments.

3.5.2. Reaction rim pyroxene composition

Pyroxenes in the reaction rims varied systematically across different experimental conditions. Under heating alone, most microlites were Mgenriched and fell near the enstatite–pigeonite boundary (Fig. 8c), although a few contained higher Ca contents and plotted in the augite field. In contrast, CO_2 flushing produced a range of pyroxene compositions with a distinct linear trend from augite through pigeonite to ferrosilite (Fig. 8d). When heating was combined with CO_2 flushing, pyroxene compositions spanned a broader range, encompassing diopside, augite, pigeonite and enstatite (Fig. 8e), reflecting the dual influence of both variables. Under elevated fO_2 (RRO), pyroxene was rare and exhibited low Ca contents and elevated Mg content relative to Fe, plotting in the enstatite field (Fig. 8f).

4. Discussion

4.1. Interpreting amphibole reaction rim textures

Our results show that heating, decompression, CO₂ flushing and redox shifts can produce characteristic textural and mineralogical signatures in amphibole reaction rims, highlighting the diagnostic roles of

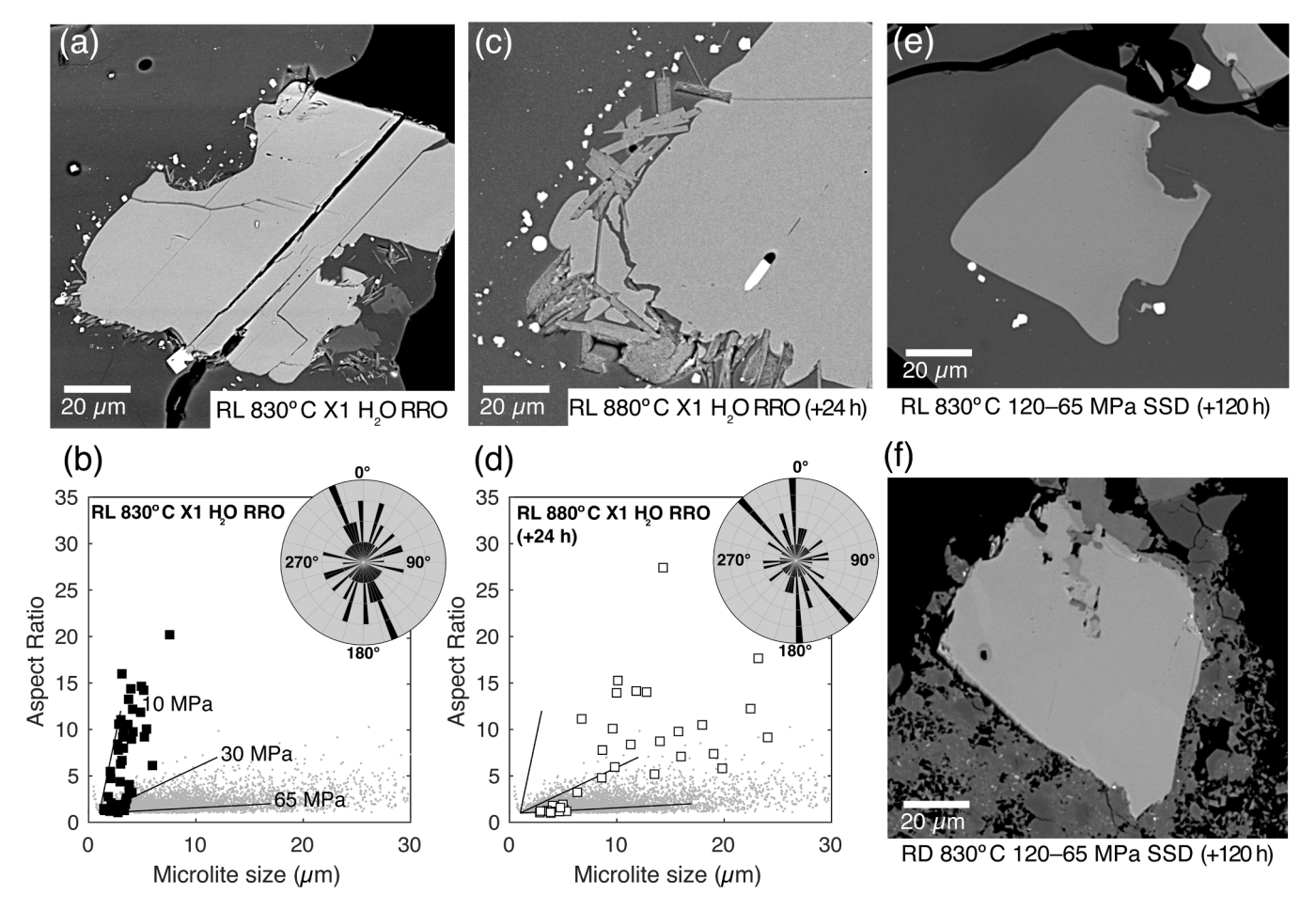


Fig. 6. Influence of changing oxygen fugacity (fO_2) on amphibole breakdown textures in a rhyolite melt. (a) Backscatter electron (BSE) image showing amphibole breakdown with fO_2 buffer NNO+2 (RRO) under baseline conditions (830 °C, 120 MPa, XH₂O = 1). (b) Quantitative textural analysis of reaction rim microlites produced at RRO conditions. (c) Multi-variable experiment showing the combined influence of increasing fO_2 (RRO) and heating to 880 °C for 24 h, characterised by the development of coarse-grained, biotite lathes and Fe-Ti oxides. (d) Quantitative textural analysis of reaction rim microlites showing microlite size against aspect ratio, alongside preferential microlite orientation relationships displayed in the inset rose diagrams. (e-f) BSE images of amphibole crystals following single-step decompression experiments from 120 to 65 MPa and holding at final pressure for 5 days (120 h), performed in a rhyolite (RL) and rhyodacite (RD) melt. These results are contextualised through comparison with previously published textural data from heating-induced breakdown experiments (light grey dots; De Angelis et al., 2015) and decompression studies conducted at various final pressures (grey lines; 10, 30 and 65 MPa; Browne and Gardner, 2006).

microlite size, aspect ratio, crystallographic orientation and mineralogy in revealing magmatic processes. Although rim thickness and mineralogy have previously been proposed to distinguish heating- from decompression-induced rims, thickness alone proves to be an unreliable indicator, because rims produced by different processes overlap in thickness (Fig. 7b,c).

Microlite size and aspect ratio offer a potentially more robust initial diagnostic tool. CO2-induced breakdown consistently yielded finegrained, acicular microlites with high aspect ratios, whereas heating favours larger, more equant crystals. Decompression-induced rims appear more complex, because their textures vary with the degree of undercooling (ΔT ; Browne and Gardner, 2006). At high ΔT , decompression produces small, high-aspect-ratio microlites similar to CO_2 -flushed rims; at low ΔT , the larger, low-aspect-ratio microlites resemble heating-induced rims (De Angelis et al., 2015). Our results suggest that crystallographic orientation may further distinguish the formation mechanism. CO₂-triggered rims typically contain microlites amphibole strongly aligned parallel to c-axis, decompression-induced rims display random orientations at any ΔT (Rutherford and Hill, 1993; Browne and Gardner, 2006). Amphibole breakdown has been proposed as a topotactic reaction, in which microlites forming within the rim inherit aspects of the crystallographic structure of the parent amphibole (De Angelis et al., 2015). The contrasting orientation relationships observed between CO_2 -induced and decompression-induced reaction rims may therefore reflect differences in the rate or timescale of amphibole breakdown. Specifically, the development of crystallographic alignment in CO_2 -triggered rims may result from more rapid breakdown (\leq 24 h), whereas the absence of such alignment in decompression experiments may indicate slower reaction kinetics operating over longer timescales (>3 days).

When texture alone is inconclusive, defining the mineralogy becomes essential. Heating and CO₂-induced rims are both pyroxene-dominated but differ in Ca content: heating produces more low-Ca pyroxenes (i.e., orthopyroxene), while CO₂ promotes high-Ca varieties (i.e., clinopyroxene). Decompression-induced rims typically contain low-Ca orthopyroxenes (Rutherford and Hill, 1993; Browne and Gardner, 2006). Even in hybrid scenarios, such as simultaneous heating and CO₂ flushing, mineralogy reveals mixed pyroxene compositions, reflecting the combined influence of these triggers.

 $f{\rm O}_2$ adds another dimension to rim interpretation. Under high $f{\rm O}_2$ (RRO), rims develop biotite-rich assemblages, with or without heating, demonstrating the important role of redox. Consequently, $f{\rm O}_2$ should be assessed first, followed by textural features and pyroxene compositions to determine the primary breakdown trigger.

Melt composition also plays a key role, mainly by affecting rim thickness and texture. The absence of reaction rims in CO_2 -flushed or

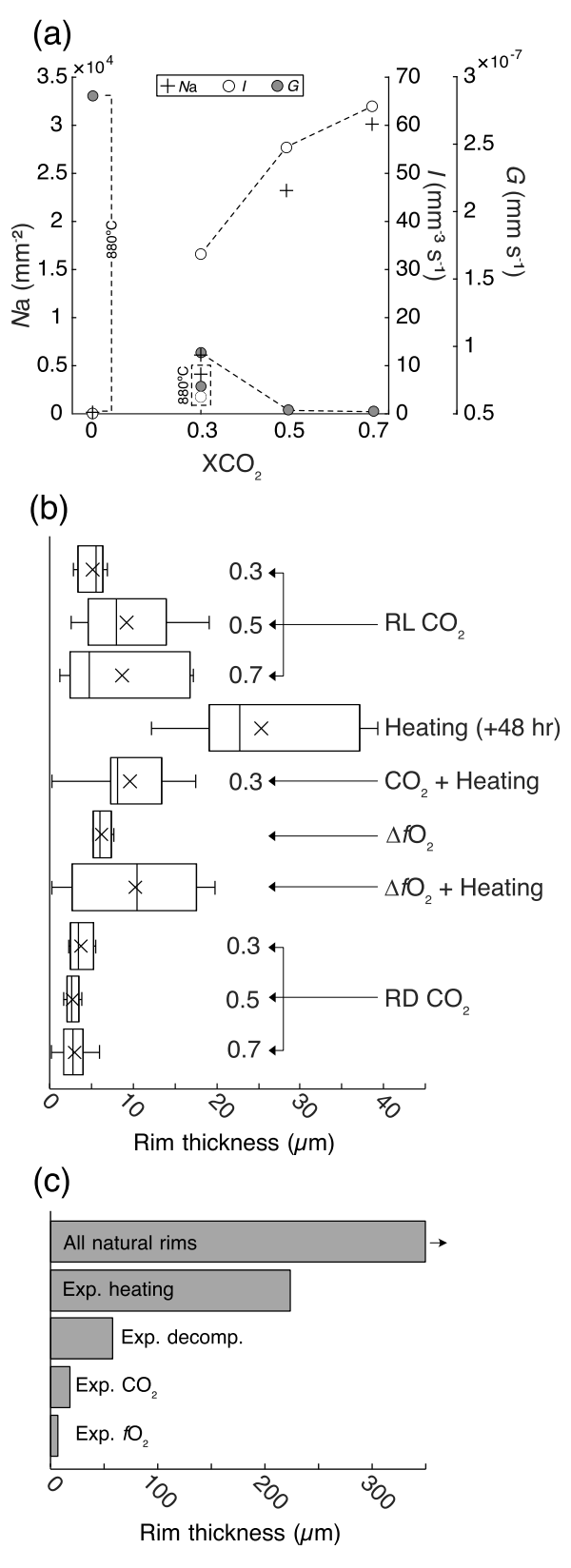


Fig. 7. Quantitative synthesis of amphibole breakdown kinetics across experimental conditions. (a) Systematic comparison of reaction rim microlite characteristics, including number density (Na), nucleation rates (I) and crystal growth rates (G) measured across varying experimental conditions ($XCO_2 = 0.3$ –0.7) and heating experiments in rhyolite melts. The data reveal systematic variations in crystallisation kinetics as a function of destabilisation mechanism. (b) Analysis of reaction rim thickness development in rhyolite (RL) and rhyodacite (RD) under different experimental conditions, demonstrating the relative efficiency of amphibole breakdown in response to CO_2 addition, temperature increase and redox variations. (c) Integration of all known experimental reaction rim thickness measurements from decompression (Rutherford and Hill, 1993; Rutherford and Devine, 2003; Rutherford and Ru

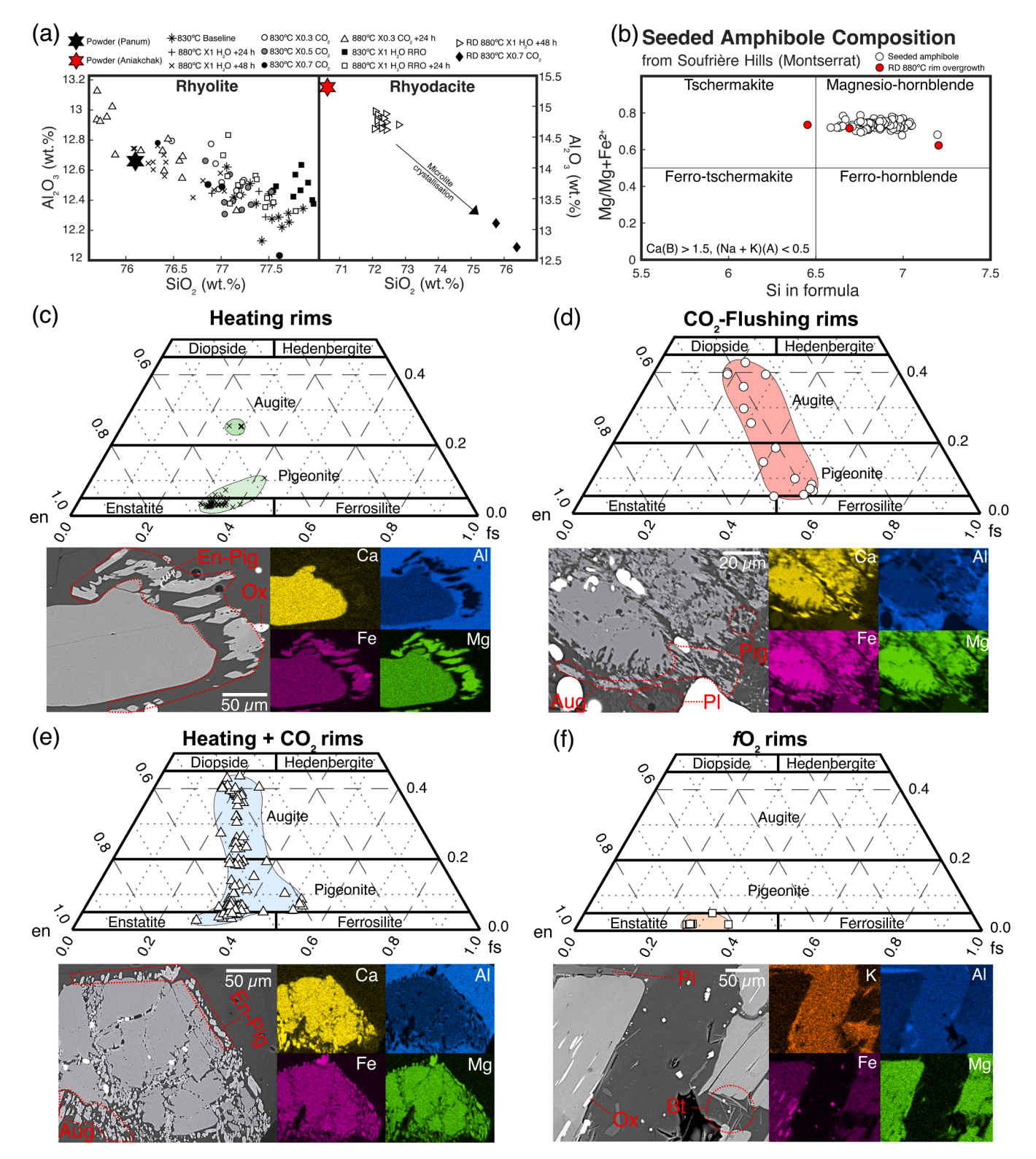


Fig. 8. Chemical evolution of experimental products across varying destabilisation conditions. (a) Major element trends in interstitial glass compositions (SiO₂ vs. Al₂O₃) from rhyolitic and rhyodacitic experiments, tracked against initial starting powder compositions, showing melt evolution during amphibole breakdown. (b) Classification of amphibole compositions following the scheme of Leake et al. (1997) using 13-cation normalisation, showing compositional ranges of seeded magnesio-hornblende amphiboles across all experiments and newly formed amphibole overgrowths from rhyodacite heating experiments, demonstrating compositional continuity between natural and experimental amphiboles. (c-f) Reaction rim pyroxene compositions plotted in classification quadrants, comparing microlites formed during: (c) heating, (d) CO₂ flushing, (e) combined heating and CO₂ flushing, and (f) elevated oxygen fugacity (RRO) conditions. Accompanying backscatter electron (BSE) images and energy-dispersive X-ray spectroscopy (EDS) elemental maps illustrate spatial variations in reaction rim mineralogy, notably the variations in low-Ca and high-Ca pyroxenes and the formation of biotite under more oxidising conditions.

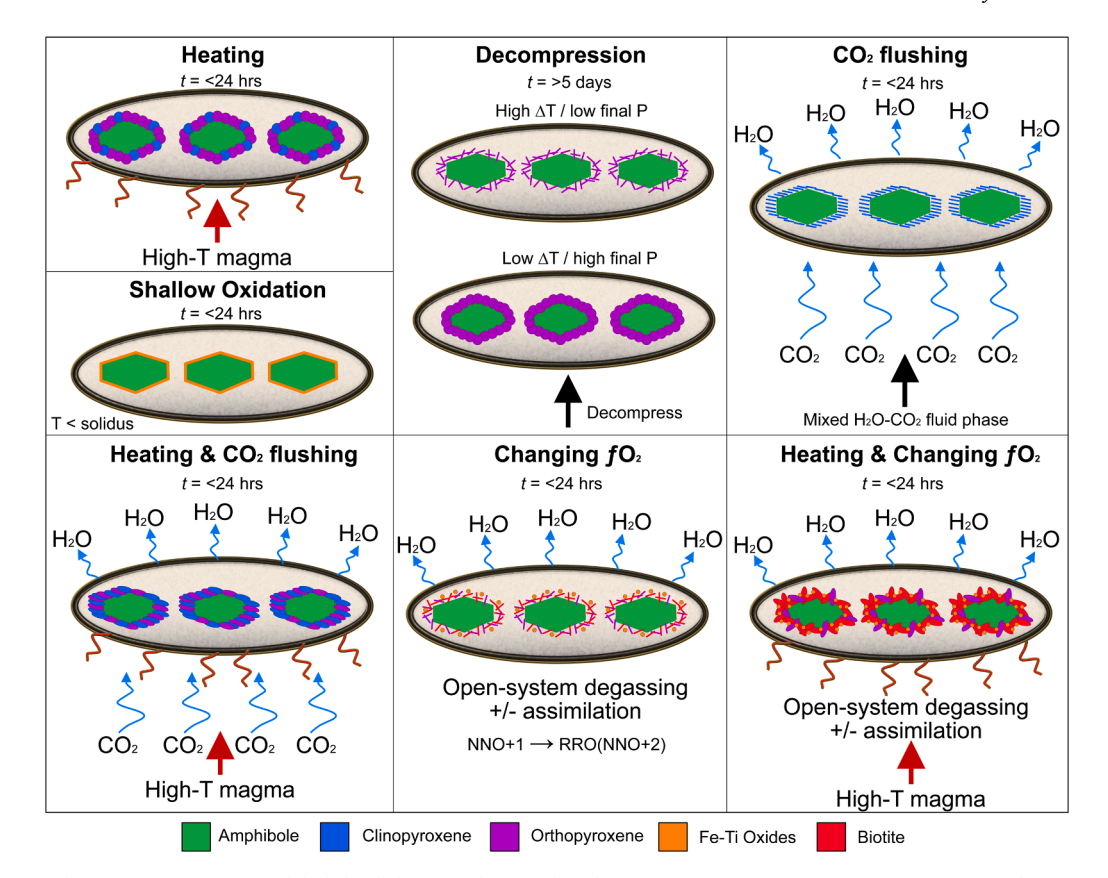


Fig. 9. Classification scheme for interpreting amphibole breakdown mechanisms based on reaction rim textures. Systematic experimental investigation of individual destabilisation mechanisms (decompression, heating, CO_2 flushing, changes in fO_2) show they each produce distinctive textural and mineralogical signatures in reaction rims, while multi-variable perturbations generate hybrid textures combining characteristics of multiple breakdown processes. This experimentally-calibrated classification framework provides a basis for interpreting breakdown mechanisms in natural systems, though application requires consideration of additional complexities in volcanic systems including varying melt compositions and the potential for multiple, concurrent or sequential destabilisation processes.

heated rhyodacite experiments, unlike the rhyolite equivalents, indicates that amphibole–melt compositional relationships can suppress rim formation. Thus, interpretations should account for both melt composition and oxidation state when determining whether heating, decompression, CO₂ flushing or hybrid processes drove amphibole breakdown.

This new interpretative framework provides a practical approach for determining the cause of amphibole breakdown in natural systems (Fig. 9). However, these experimental textural and mineralogical signatures represent end-member and simultaneously operating processes, with the latter more likely in natural systems. Moreover, natural systems commonly involve sequential processes that can produce zoned reaction rim textures. Therefore, natural reaction rim textures require careful evaluation of the full suite of diagnostic features for accurate interpretation. Ultimately, the key to successful interpretation lies in the systematic assessment of microlite size, aspect ratio, orientation and mineralogy across the full transect of the rim, while also considering the potential effects of undercooling, redox state and melt composition.

4.2. Amphibole reaction rims as a record of pre-eruptive volatile fluctuations

After H₂O, CO₂ is the second most abundant magmatic volatile across diverse melt compositions (e.g., Lowenstern, 2001; Wallace, 2005). As CO₂ is less soluble than H₂O, it exsolves preferentially during ascent, leaving shallow silicic melts highly depleted in CO₂ but saturated in H₂O (Fig 1b; Papale and Polacci, 1999; Newman and Lowenstern, 2002; Wallace, 2005; Ghiorso and Gualda, 2015; Edmonds et al., 2022). Moreover, CO₂ may be introduced into shallow silicic magmas, typically as a fluid phase, when interacting with primitive basaltic magmas (e.g.,

Papale and Polacci, 1999; Roberge et al., 2009; Blundy et al., 2010), which commonly contain substantial CO₂, or if carbonate host rocks calcinates (Deegan et al., 2010; Dallai et al., 2011; Preece et al., 2014; Mason et al., 2017; Arzilli et al., 2023). As this CO₂-bearing fluid interacts with shallow silicic melts, it triggers significant H₂O exsolution and minor CO₂ dissolution (Fig. 1c), often resulting in dynamic crystallisation (Cashman and Blundy, 2013; Rader and Larsen, 2013; Riker et al., 2015; Giuffrida et al., 2017).

Our experiments show that CO_2 can strongly destabilise amphibole in shallow magma reservoirs, as revealed by systematic increases in Na and preferential microlite alignment, along with an increase in crystal nucleation rates (I) and decrease in growth rate (G) in the reaction rims (Fig. 3 and Fig. 7a). Reducing $\mathrm{H}_2\mathrm{O}$ activity and creating local chemical potential gradients enhance I (Papale and Polacci, 1999; Lowenstern, 2001; Blundy et al., 2010), while the persistent alignment of microlites with parent amphibole crystallographic planes suggests topotactic growth. The dominant occurrence of clinopyroxene and minor Fe-Ti oxides in CO_2 -driven rims contrasts with other breakdown mechanisms (Fig. 8d), affirming the key role of CO_2 flushing in amphibole destabilisation.

This process likely sets up transient chemical gradients and can release latent heat, mirroring thermal instabilities associated with decompression-induced crystallisation (Blundy et al., 2006; Caricchi et al., 2018). Monitoring CO_2 in magmatic systems commonly relies on gas emissions (Mason et al., 2017; Edmonds et al., 2022) and volatile contents in the groundmass glass and melt inclusions (Wallace, 2005; Blundy et al., 2010). Combining these approaches with mineral textures, such as those of amphibole reaction rims, offers a powerful means to track CO_2 fluctuations through the crust.

While our experiments show that CO2 can destabilise amphibole

under shallow crustal conditions, this effect is likely depth- and composition-dependent. Amphibole stability in silicic melts requires dissolved H₂O concentrations of typically ≥3.5–4.0 wt. % (e.g., Eggler and Burnham, 1973; Holloway, 1973), and the reduction of melt H₂O below this threshold by CO2 influx would require substantial fluid volumes, particularly at small to moderate XCO2 values (Ghiorso and Gualda, 2015). Volatiles by difference values derived from EPMA totals of the experimental glasses (following the approach of Hughes et al. (2019); see Electronic Supplementary Material) are consistent with amphibole breakdown in the presence of CO2 occurring near the lower H₂O stability limit (<3 wt. % H₂O) supporting this interpretation. Such conditions are more easily achieved in magmas that have already ascended into the upper crust, where pressure-limited H₂O solubility makes amphibole less stable. Thus, CO2-induced amphibole breakdown is most likely to occur in magmas that have already ascended into the shallow crust, and may be less effective at greater depths where melts remain strongly H₂O-saturated.

Studies have shown that injection of CO_2 into shallow crustal magma chambers may significantly alter magma properties and promote explosive eruptions (e.g., Caricchi et al., 2018; Feignon et al., 2022). The 2009 Redoubt Volcano eruption illustrates this phenomenon: elevated CO_2 flux occurred weeks before the March 15 eruption (Werner et al., 2013), and a circulating vapor phase of \sim 75 mol. % H_2O and 25 mol. % CO_2 was identified in upper crustal storage zones (Coombs et al., 2013). Amphiboles in the early eruptive products formed distinct reaction rims attributed to H_2O -driven decompression (Coombs et al., 2013). However, our findings suggest that $XCO_2 = 0.25$ is sufficient to destabilise amphibole at upper crustal pressures, indicating that CO_2 -rich vapor phases should not be ruled out in amphibole breakdown scenarios at volcanoes with evidence for an excess fluid phase if volumes are sufficient (e.g., from melt inclusions or gas monitoring data).

4.3. Thermal destabilisation of magma

In volcanic systems, heating commonly occurs during the recharge of high-temperature magma (Sparks and Marshall, 1986), but also via crystallisation (Blundy et al., 2006) and shear associated with ascent (Lavallée et al., 2015), transferring heat and destabilising amphibole. Pre-eruptive magma recharge has been inferred at Soufrière Hills Volcano (e.g., Murphy et al., 2000), Unzen (Nakada and Motomura, 1999), Ciomadul (Kiss et al., 2014), Bezymyannyi (Plechov et al., 2008) and Merapi (Erdmann et al., 2014). Our heating experiments replicate the textures typical of such recharge events (Fig. 5c,d) and differ markedly from those generated by CO₂ (Fig. 3a,b). Prolonged heating at 880 °C for 48 h produced thick, coarse-grained rims dominated by blocky, low-aspect-ratio microlites with preferential orientations. These rims contain high-Mg, low-Ca pyroxenes (± minor high-Ca pyroxene; Fig. 8c), reflecting enhanced diffusion rates at elevated temperatures that favour Mg incorporation and the formation of more equant, thermally stable phases compared to CO2-driven rims. These findings confirm earlier interpretations of heating-induced rims (Rutherford and Devine, 2003; De Angelis et al., 2015).

At Unzen Volcano, granular and symplectitic reaction rims in amphiboles within the dome products have been attributed to magma mixing (Nakada and Motomura, 1999) and/or localised heating via shear/frictional processes (Wallace et al., 2019). The resemblance of our experimental textures to those at Unzen underscores the applicability of our results to natural systems. Similarly, at Soufrière Hills, thick, coarse-grained rims dominated by clinopyroxene, orthopyroxene and Fe-Ti oxides have been linked to repeated recharge and heating events (Barclay et al., 1998; Murphy et al., 2000; Rutherford and Devine, 2003), closely matching the textures observed in our heating experiments.

Previous studies that identified pre-eruptive heating based on petrological evidence often assume a purely thermal origin for amphibole rims, with little consideration of simultaneous volatile interactions. Our combined CO_2 —heating experiments yield hybrid textures with features of both CO_2 -driven and thermally-induced rims (Fig. 5e,f). The resulting pyroxenes cover a broad compositional range from Ca- to Mgrich, while retaining notable Fe enrichment (Fig. 8e). These observations highlight the complexity of natural magmatic systems, where concurrent processes (particularly in recharge events) can lead to more diverse reaction rim textures and mineral compositions than either process would produce alone.

4.4. Role of fO₂ in amphibole stability

Our experiments show that oxygen fugacity (fO2) can critically influence amphibole stability and reaction rim textures in silicic magmas. Under more oxidising conditions (RRO), amphibole breakdown yielded thin, fine-grained, randomly oriented microlites dominated by biotite, low-Ca pyroxene and Fe-Ti oxides (Fig. 6a,b). This outcome differs markedly from other breakdown conditions and reflects how redox state controls Fe speciation, crystal chemistry and phase equilibria (e.g., Burgisser and Scaillet, 2007; Moussallam et al., 2014). The biotite-rich rims at high fO2 demonstrate that oxidising conditions favour Fe³⁺-bearing phases at the expense of Fe²⁺-rich minerals (Toplis and Carroll, 1995; Frost and McCammon, 2008). As a result, Mg-rich pyroxenes likely arise because less Fe²⁺ is available. These compositional differences underscore how changes in fO2 alone can drastically alter amphibole reaction rim assemblages and offer a potential means of reconstructing magmatic redox states (Tollan and Hermann, 2019; Sun and Lee, 2022). It is important to note that the breakdown of amphibole observed in our experiments reflects the specific composition of the magnesio-hornblende used as a starting material, derived from Soufrière Hills Volcano. Amphiboles from more oxidised magmas (e.g., El Chichón, Pinatubo, or the Fish Canyon Tuff) may exhibit greater stability at higher fO2, even under conditions near the magnetite-hematite buffer (Luhr, 1990). Thus, the destabilisation of amphibole from NNO+1 to RRO in our study should not be taken as universally representative, but rather compositionally dependent.

Natural magmatic systems experience redox fluctuations driven by processes such as magma mixing, crustal assimilation, crystallisation of Fe-bearing phases, volatile fluxing and degassing (e.g., Carmichael, 1991; Sun and Lee, 2022). Variations in fO_2 can thus serve as a stand-alone trigger for rim formation, especially in arc volcanoes subject to repeated injections of oxidised fluids (e.g., Kiss et al., 2014), consequently impacting the rheological properties of magma (Dingwell and Virgo, 1987; Kolzenburg et al., 2018). Near-surface oxidation can further promote the formation of fine-grained, Fe-Ti oxide-rich rims, a common feature of dome-building systems (Garcia and Jacobson, 1979; Plechov et al., 2008; Wallace et al., 2019).

At Ciomadul Volcano, Kiss et al. (2014) recorded amphibole zonation attributed to decompression, heating and variable fO_2 . Our isobaric–isothermal experiments confirm that changing fO_2 can affect amphibole stability significantly. Unzen Volcano provides another example: the various lobes that form the lava dome contain widespread biotite breakdown, forming pargasitic amphibole in its rim products (Nakada and Motomura, 1999). This observation suggests that if biotite experiences heating and reduction with minimal H_2O exsolution, as was interpreted (Venezky and Rutherford, 1999), Fe^{3+} transforms into Fe^{2+} , favouring amphibole formation. Our experiments show the reverse reaction is also possible, where elevated fO_2 conditions drive amphibole breakdown to biotite, with combined fO_2 shifts and heating producing hybrid rim textures (Fig. 6c,d). The redox state exerts a primary influence on mineral assemblage, while temperature predominantly affects crystal size and morphology.

4.5. Insights into decompression and magma ascent

Decompression inevitably accompanies magma ascent, lowering volatile solubility in the melt and rendering amphibole unstable if the

magma ascends to sufficiently shallow depths or erupts (Fig. 1b). Early studies by Rutherford and Hill (1993) showed that decompression-induced rims typically consist of acicular orthopyroxene microlites, which can serve as proxies for ascent rates. This mechanism has been widely documented in amphibole-bearing dacites at Mount St. Helens (Rutherford and Hill, 1993), Soufrière Hills Volcano (Rutherford and Devine, 2003) and Redoubt Volcano (Browne and Gardner, 2006), where the degree of undercooling and final storage pressure notably influence rim textures. More recent work indicates that $\rm CO_2$ -rich vapor fluxing may also destabilise amphibole by dehydrating the melt, as evidenced by complex plagioclase zoning and elevated $\rm CO_2$ in melt inclusions at Mount St. Helens (e.g., Cashman and Blundy, 2013).

In our decompression experiments, pressure was reduced from 120 MPa to 65 MPa and was held at final pressure for 5 days. Although amphibole in the rhyolite runs showed partial resorption (Fig. 6e,f), no reaction rims formed. This outcome does not contradict the established role of decompression in amphibole breakdown but highlights the importance of ascent rate, extent and duration of pressure reduction, final storage pressure (if magma stalls during ascent or erupts at once), and melt composition (Rutherford and Hill, 1993; Browne and Gardner, 2006). Previous decompression experiments (Browne and Gardner, 2006) produced rims within 3–4 days even at final pressures of 65 MPa, likely a result of different undercooling paths (e.g., higher starting pressures) or melt compositions that were more conducive to rim formation, suggesting that small changes in ascent conditions can significantly influence kinetic pathways, underscoring how different timescales and conditions drive distinct breakdown mechanisms.

4.6. Role of melt composition in amphibole stability

Our experiments show that melt composition strongly influences amphibole stability and reaction rim development, with marked differences between rhyolitic and rhyodacitic compositions. Under the same heating conditions, amphiboles in rhyolitic melts developed substantial rims, whereas those in rhyodacitic melts remained stable and even showed overgrowth (Fig. 8b; Fig. S1b), highlighting how melt structure and chemical potentials can override other destabilising factors and profoundly affect phase equilibria. Moreover, amphibole breakdown itself feeds back on melt composition by releasing Fe, Mg and Ca into the interstitial melt, thereby modifying its chemistry in a direction that may influence subsequent phase equilibria (Fig. S2). These results underscore the bidirectional coupling between amphibole stability and melt composition, with implications for both the kinetics and pathways of melt evolution in hydrous silicic systems.

In natural systems, melt composition commonly evolves through fractional crystallisation typically creating more silicic, MgO- and FeO-depleted melts (e.g., Ghiorso and Gualda, 2015). These processes can be further complicated by magma mixing or assimilation events that generate hybrid melt compositions, introducing complex phase stability relationships (Sparks and Marshall, 1986; Murphy et al., 2000; Morgavi et al., 2013). The extensive groundmass crystallisation observed in rhyodacitic experiments, especially at higher CO₂ concentrations, highlights how melt composition can control crystallisation kinetics (e.g., Brugger and Hammer, 2010). Such compositional shifts can produce feedback loops, enhancing or hindering amphibole breakdown, and may help explain the texturally zoned amphibole rims often noted in natural samples (e.g., McCanta et al., 2007; Plechov et al., 2008).

As reaction rim formation depends on melt composition as well as pressure and temperature, interpretations based solely on single variables risk oversimplification. A comprehensive approach that includes melt compositional effects is thus essential for deciphering the information preserved in rim textures. This expanded framework would reconcile contradictory interpretations from volcanic systems and produce more robust indicators of pre-eruptive processes. Such steps are critical given that amphibole reaction rims can preserve evidence of magmatic evolution on timescales relevant to volcanic hazard

assessment.

5. Implications and conclusions

The results presented here provide new perspectives on amphibole reaction rim formation and its importance for interpreting pre-eruptive magmatic processes. By systematically examining the roles of $\rm CO_2$ flushing, $\rm fO_2$, heating and decompression on amphibole stability in two high-silica melts—a rhyolite (76.1 wt. % $\rm SiO_2$) and a rhyodacite (70.6 wt. % $\rm SiO_2$)—we have shown that each control imparts distinct textural and mineralogical signatures in amphibole reaction rims, which can be distinguished even when acting simultaneously. This outcome moves beyond the traditional focus on single triggers, underscoring the complexity of amphibole breakdown and highlighting the significant influence of volatile interactions (particularly $\rm CO_2$) and redox conditions.

Recognising these distinct reaction rim signatures has important implications for volcanic hazard assessment. In natural systems, differentiating between textures produced by CO_2 influx, heating, decompression or changing oxidation conditions can refine our ability to interpret shifts in magma storage and ascent conditions. The strong role of CO_2 flushing, in particular, suggests that rim textures can record volatile influx events, aligning with independent evidence from gas emissions or melt inclusion studies. Likewise, the biotite-rich rims formed under high $f\mathrm{O}_2$ conditions indicate that shifts in redox state alone can be sufficient to destabilise amphibole. Combining reaction rim analyses with geochemical monitoring, such as real-time gas flux measurements and melt inclusion compositions, may therefore offer a more robust means of identifying and tracking the processes that lead to eruptions.

Collectively, our experiments emphasise that amphibole stability in silicic magmas is governed by the combined effects of temperature, pressure, melt composition and redox state, each of which plays a critical and often interdependent role in destabilising amphibole. While decompression remains a well-documented mechanism of amphibole breakdown, our findings highlight how under certain conditions—especially those involving slower ascent rates, specific melt compositions or significant $\rm CO_2$ concentrations—reaction rims may be absent or develop differently. Heating experiments confirm that prolonged high temperatures can produce distinct blocky, low-Ca pyroxene rims, while elevated $\rm fO_2$ conditions can yield thin, biotite-dominated rims. The capacity of $\rm CO_2$ alone to induce strongly oriented, accicular microlites demonstrates how even short-lived volatile flushing can destabilise amphibole.

By refining our capacity to interpret these indicators, this study refines petrological models of magma storage and ascent, contributing an essential tool for future volcanic hazard assessment efforts. More comprehensive monitoring programs that integrate crystal texture analyses, gas flux observations and melt inclusion geochemistry will help reveal the interplay between multiple processes in the final stages before eruption. Such an integrated approach promises a deeper understanding of how amphibole breakdown mirrors critical transitions in magma evolution, ultimately enhancing eruption forecasting and potentially contributing to the development of eruption style prediction methods.

CRediT authorship contribution statement

Paul A. Wallace: Writing – review & editing, Writing – original draft, Visualization, Validation, Project administration, Methodology, Investigation, Funding acquisition, Formal analysis, Data curation, Conceptualization. Sarah H. De Angelis: Writing – review & editing, Methodology, Investigation, Formal analysis, Data curation, Conceptualization. Jessica Larsen: Writing – review & editing, Supervision, Resources, Methodology, Funding acquisition, Conceptualization. Luca Caricchi: Writing – review & editing, Validation, Resources, Funding acquisition, Conceptualization. Jackie E. Kendrick: Writing – review &

editing, Conceptualization. Yan Lavallée: Writing – review & editing, Supervision, Funding acquisition, Conceptualization.

Declaration of competing interest

The authors declare that they have no known competing financial interests or personal relationships that could have appeared to influence the work reported in this paper.

Acknowledgments

The authors are indebted to Ken Severin (University of Alaska Fairbanks), Florence Bégué (University of Geneva), Nathan Graham (University of Alaska Fairbanks), Dirk Mueller (LMU Munich), and Toby Swift for assistance during analytical data collection. We thank the Inyo National Forest Service of the United States Department of Agriculture to permit sampling at Panum crater, USA. We kindly acknowledge the following funding support: PW – Liverpool Doctoral Scholarship and LMUexcellent fund, funded by the Federal Ministry of Education and Research (BMBF) and the Free State of Bavaria under the Excellence Strategy of the Federal Government and the Länder; JL - National Science Foundation (NSF) grant EAR-1650185; LC - Swiss National Science Foundation grant no. 200021_184632; YL - European Research Council (ERC) MODERATE project grant no. 101001065 and LMUexcellent fund. We wish to thank the editor, C. Petrone, and two reviewers P. Shane and T. Sisson for their insightful, detailed and constructive reviews.

Supplementary materials

Supplementary material associated with this article can be found, in the online version, at doi:10.1016/j.epsl.2025.119532.

Data availability

Data will be made available on request.

References

- Aiuppa, A., Fischer, T.P., Plank, T., Bani, P., 2019. CO2 flux emissions from the Earth's most actively degassing volcanoes, 2005-2015. Sci. Rep. 9, 5442.
- Andrews, B.J., 2014. Magmatic storage conditions, decompression rate, and incipient caldera collapse of the 1902 eruption of Santa Maria Volcano, Guatemala. J. Volcanol. Geotherm. Res. 282, 103–114.
- Arzilli, F., Burton, M., La Spina, G., Macpherson, C.G., van Keken, P.E., McCann, J., 2023. Decarbonation of subducting carbonate-bearing sediments and basalts of altered oceanic crust: insights into recycling of CO2 through volcanic arcs. Earth Planet. Sci. Lett. 602, 117945.
- Barclay, J., Rutherford, M.J., Carroll, M.R., Murphy, M.D., Devine, J.D., Gardner, J., et al., 1998. Experimental phase equilibria constraints on preemptive storage conditions of the Soufriere Hills magma. Geophys. Res. Lett. 25, 3437–3440.
- Blundy, J., Cashman, K., Humphreys, M., 2006. Magma heating by decompression-driven crystallization beneath andesite volcanoes. Nature 443, 76–80.
- Blundy, J., Cashman, K.V., Rust, A., Witham, F., 2010. A case for CO2-rich arc magmas. Earth Planet. Sci. Lett. 290, 289–301.
- Browne, B.L., Gardner, J.E., 2006. The influence of magma ascent path on the texture, mineralogy, and formation of hornblende reaction rims. Earth Planet. Sci. Lett. 246, 161–176.
- Brugger, C.R., Hammer, J.E., 2010. Crystallization kinetics in continuous decompression experiments: implications for interpreting natural magma ascent processes. J. Petrol. 51, 1941–1965.
- Buckley, V.J.E., Sparks, R.S.J., Wood, B.J., 2006. Hornblende dehydration reactions during magma ascent at Soufriere Hills Volcano, Montserrat. Contrib. Mineral. Petrol. 151, 121–140.
- Burgisser, A., 2003. Magmas in Motion: Degassing in Volcanic Conduits and Fabrics of Pyroclastic Density Current. Alaska: University of Alaska, Fairbanks.
- Burgisser, A., Scaillet, B., 2007. Redox evolution of a degassing magma rising to the surface. Nature 445, 194–197.
- Burton, M.R., Sawyer, G.M., Granieri, D., 2013. Deep carbon emissions from volcanoes. Rev. Mineral. Geochem. 75, 323–354.
- Caricchi, L., Sheldrake, T.E., Blundy, J., 2018. Modulation of magmatic processes by CO2 flushing. Earth Planet. Sci. Lett. 491, 160–171.
- Carmichael, I.S.E., 1991. The redox states of basic and silicic magmas: a reflection of their source regions? Contrib. Mineral. Petrol. 106, 129–141.

- Carmichael, I.S.E., Ghiorso, M.S., 1990. Chapter 7 the effect of oxygen fugacity on the redox state of natural liquids and their crystallizing phases. In: Nicholls, J., Russell, K. (Eds.), Modern Methods of Igneous Petrology. De Gruyter, Berlin, Boston, pp. 191–212.
- Cashman, K., Blundy, J., 2013. Petrological cannibalism: the chemical and textural consequences of incremental magma body growth. Contrib. Mineral. Petrol. 166, 703–729
- Cashman, K.V., Sparks, R.S.J., Blundy, J.D., 2017. Vertically extensive and unstable magmatic systems: A unified view of igneous processes. Science 355.
- Coombs, M.L., Sisson, T.W., Bleick, H.A., Henton, S.M., Nye, C.J., Payne, A.L., et al., 2013. Andesites of the 2009 eruption of Redoubt Volcano, Alaska. J. Volcanol. Geotherm. Res. 259, 349–372.
- Dallai, L., Cioni, R., Boschi, C., D'Oriano, C., 2011. Carbonate-derived CO2 purging magma at depth: influence on the eruptive activity of Somma-Vesuvius, Italy. Earth Planet. Sci. Lett. 310. 84–95.
- De Angelis, S.H., Larsen, J., Coombs, M., 2013. Pre-eruptive magmatic conditions at Augustine volcano, Alaska, 2006: Evidence from amphibole geochemistry and textures. Journal of Petrology 54, 1939–1961.
- De Angelis, S.H., Larsen, J., Coombs, M., Dunn, A., Hayden, L., 2015. Amphibole reaction rims as a record of pre-eruptive magmatic heating: an experimental approach. Earth Planet. Sci. Lett. 426, 235–245.
- Deegan, F.M., Troll, V.R., Freda, C., Misiti, V., Chadwick, J.P., McLeod, C.L., et al., 2010.
 Magma–carbonate interaction processes and associated CO2 release at merapi volcano, Indonesia: insights from experimental petrology. J. Petrol. 51, 1027–1051.
- Devine, J.D., Rutherford, M.J., Gardner, J.E., 1998. Petrologic determination of ascent rates for the 1995-1997 Soufriere Hills Volcano andesitic magma. Geophys. Res. Lett. 25, 3673–3676.
- Dingwell, D.B., Virgo, D., 1987. The effect of oxidation state on the viscosity of melts in the system Na2O-FeO-Fe2O3-SiO2. Geochim. Cosmochim. Acta 51, 195–205.
- D'Mello, N.G., Zellmer, G.F., Negrini, M., Kereszturi, G., Procter, J., Stewart, R., et al., 2021. Deciphering magma storage and ascent processes of Taranaki, New Zealand, from the complexity of amphibole breakdown textures. Lithos 398–399, 106264.
- Edmonds, M., Liu, E.J., Cashman, K.V., 2022. Open-vent volcanoes fuelled by depthintegrated magma degassing. Bull. Volcanol. 84.
- Eggler, D.H., Burnham, C.W., 1973. Crystallization and fractionation trends in the system
 Andesite-H2O-CO2-O2 at pressures to 10 kb. Geol. Soc. Am. Bull. 84, 2517.
- Erdmann, S., Martel, C., Pichavant, M., Kushnir, A., 2014. Amphibole as an archivist of magmatic crystallization conditions: problems, potential, and implications for inferring magma storage prior to the paroxysmal 2010 eruption of Mount Merapi, Indonesia, Contrib. Mineral. Petrol. 167, 1–23.
- Eugster, H.P., 1957. Heterogeneous reactions involving oxidation and reduction at high pressures and temperatures. J. Chem. Phys. 26, 1760–1761.
- Feignon, J.-G., Cluzel, N., Schiavi, F., Moune, S., Roche, O., Clavero, J., et al., 2022. High CO2 content in magmas of the explosive andesitic Enco eruption of Mocho-Choshuenco volcano (Chile). Bull. Volcanol. 84.
- Frost, D.J., McCammon, C.A., 2008. The redox state of earth's mantle. Annu. Rev. Earth Planet. Sci. 36, 389–420.
- Garcia, M.O., Jacobson, S.S., 1979. Crystal clots, amphibole fractionation and the evolution of calc-alkaline magmas. Contrib. Mineral. Petrol. 69, 319–327.
- Ghiorso, M.S., Gualda, G.A.R., 2015. An H2O–CO2 mixed fluid saturation model compatible with rhyolite-MELTS. Contrib. Mineral. Petrol. 169.
- Giuffrida, M., Holtz, F., Vetere, F., Viccaro, M., 2017. Effects of CO2 flushing on crystal textures and compositions: experimental evidence from recent K-trachybasalts erupted at Mt. Etna. Contrib. Mineral. Petrol. 172.
- Holloway, J.R., 1973. The system pargasite-H2O-CO2: a model for melting of a hydrous mineral with a mixed-volatile fluid—I. Experimental results to 8 kbar. Geochim. Cosmochim. Acta 37, 651–666.
- Hughes, E.C., Buse, B., Kearns, S.L., Blundy, J.D., Kilgour, G., Mader, H.M., 2019. Low analytical totals in EPMA of hydrous silicate glass due to sub-surface charging: obtaining accurate volatiles by difference. Chem. Geol. 505, 48–56.
- Hughes, E.C., Liggins, P., Saper, L., Stolper, E.M., 2024. The effects of oxygen fugacity and sulfur on the pressure of vapor-saturation of magma. Am. Mineral. 109, 422-438
- Kiss, B., Harangi, S., Ntaflos, T., Mason, P.R.D., Pál-Molnár, E., 2014. Amphibole perspective to unravel pre-eruptive processes and conditions in volcanic plumbing systems beneath intermediate arc volcanoes: a case study from Ciomadul volcano (SE Carpathians). Contrib. Mineral. Petrol. 167, 1–27.
- Kolzenburg, S., Di Genova, D., Giordano, D., Hess, K.U., Dingwell, D.B., 2018. The effect of oxygen fugacity on the rheological evolution of crystallizing basaltic melts. Earth Planet. Sci. Lett. 487, 21–32.
- La Spina, G., Burton, M., De'Michieli Vitturi, M., Arzilli, F., 2016. Role of syn-eruptive plagioclase disequilibrium crystallization in basaltic magma ascent dynamics. Nat. Commun. 7, 13402.
- Larsen, J.F., 2006. Rhyodacite magma storage conditions prior to the 3430 yBP calderaforming eruption of Aniakchak volcano, Alaska. Contrib. Mineral. Petrol. 152, 523–540.
- Lavallée, Y., Dingwell, D.B., Johnson, J.B., Cimarelli, C., Hornby, A.J., Kendrick, J.E., et al., 2015. Thermal vesiculation during volcanic eruptions. Nature 528, 544–547.
 Leake, B.E., Woolley, A.R., Arps, C.E.S., Birch, W.D., Gilbert, M.C., Grice, J.D.,
- Hawthorne, F.C., Kato, A., Kisch, H.J., Krivovichev, V.G., Linthout, K., Laird, J., Mandarino, J., Maresch, W.V., Nickel, E.H., Rock, N.M.S., Schumacher, J.C., Smith, D.C., Stephenson, N.C.N., Ungaretti, L., Whittaker, E.J.W., Youzhi, G., 1997. Nomenclature of amphiboles; Report of the subcommittee on amphiboles of the international mineralogical association commission on new minerals and mineral names. Mineralogical magazine 61, 295–310.

- Lowenstern, J.B., 2001. Carbon dioxide in magmas and implications for hydrothermal systems. Miner. Deposita 36, 490–502.
- Luhr, J.F., 1990. Experimental phase relations of water- and sulfur-saturated arc magmas and the 1982 eruptions of El Chichon volcano. J. Petrol. 31, 1071–1114.
- Mangan, M., Sisson, T., 2000. Delayed, disequilibrium degassing in rhyolite magma: decompression experiments and implications for explosive volcanism. Earth Planet. Sci. Lett. 183, 441–455.
- Mason, E., Edmonds, M., Turchyn, A.V., 2017. Remobilization of crustal carbon may dominate volcanic arc emissions. Science 357, 290–294.
- McCanta, M.C., Rutherford, M.J., Hammer, J.E., 2007. Pre-eruptive and syn-eruptive conditions in the Black Butte, California dacite: insight into crystallization kinetics in a silicic magma system. J. Volcanol. Geotherm. Res. 160, 263–284.
- Mollo, S., Hammer, J.E., 2017. Dynamic crystallization in magmas. Eur. Mineral. Union Notes Mineral. 16, 373–418.
- Morgavi, D., Perugini, D., De Campos, C.P., Ertl-Ingrisch, W., Lavallée, Y., Morgan, L., et al., 2013. Interactions between rhyolitic and basaltic melts unraveled by chaotic mixing experiments. Chem. Geol. 346, 119–212.
- Moussallam, Y., Oppenheimer, C., Scaillet, B., Gaillard, F., Kyle, P., Peters, N., et al., 2014. Tracking the changing oxidation state of erebus magmas, from mantle to surface, driven by magma ascent and degassing. Earth Planet. Sci. Lett. 393, 200–209.
- Murphy, M.D., Sparks, R.S.J., Barclay, J., Carroll, M.R., Brewer, T.S., 2000.

 Remobilization of andesite magma by intrusion of mafic magma at the Soufriere Hills volcano, Montserrat, West Indies. J. Petrol. 41, 21–42.
- Nakada, S., Motomura, Y., 1999. Petrology of the 1991-1995 eruption at Unzen: effusion pulsation and groundmass crystallization. J. Volcanol. Geotherm. Res. 89, 173–196.
- Newman, S., Lowenstern, J.B., 2002. VolatileCalc: a silicate melt–H2O–CO2 solution model written in Visual Basic for excel. Comput. Geosci. 28, 597–604.
- Papale, P., Polacci, M., 1999. Role of carbon dioxide in the dynamics of magma ascent in explosive eruptions. Bull. Volcanol. 60, 583–594.
- Pistone, M., Caricchi, L., Ulmer, P., 2021. CO 2 favours the accumulation of excess fluids in felsic magmas. Terra Nova 33, 120–128.
- Plechov, P.Y., Tsai, A.E., Shcherbakov, V.D., Dirksen, O.V., 2008. Opacitization conditions of hornblende in Bezymyannyi volcano andesites (March 30, 1956 eruption). Petrology 16, 19–35.
- Preece, K., Facility, E.I.M., Gertisser, R., Barclay, J., Berlo, K., Herd, R.A., 2014. Pre- and syn-eruptive degassing and crystallisation processes of the 2010 and 2006 eruptions of Merapi volcano, Indonesia. Contrib. Mineral. Petrol. 168.
- Rader, E.L., Larsen, J.F., 2013. Experimental phase relations of a low MgO aleutian basaltic andesite at XH2O = 0.7-1. Contrib. Mineral. Petrol. 166, 1593–1611.
- Ridolfi, F., Renzulli, A., Puerini, M., 2010. Stability and chemical equilibrium of amphibole in calc-alkaline magmas: an overview, new thermobarometric formulations and application to subduction-related volcanoes. Contrib. Mineral. Petrol. 160, 45–66.
- Riker, J.M., Cashman, K.V., Rust, A.C., Blundy, J.D., 2015. Experimental constraints on plagioclase crystallization during H2O- and H2O-CO2-saturated magma decompression. J. Petrol. 56, 1967–1998.

- Roberge, J., Delgado-Granados, H., Wallace, P.J., 2009. Mafic magma recharge supplies high CO2 and So2 gas fluxes from Popocatépetl volcano, Mexico. Geology 37, 107–110.
- Rutherford, M.J., Devine, J.D., 2003. Magmatic conditions and magma ascent as indicated by hornblende phase equilibria and reactions in the 1995-2002 Soufrière Hills magma. J. Petrol. 44, 1433–1454.
- Rutherford, M.J., Hill, P.M., 1993. Magma ascent rates from amphibole breakdown: An experimental study applied to the 1980-1986 Mount St. Helens eruptions.

 J. Geophys. Res. 98.
- Rutherford, M.J., Sigurdsson, H., Carey, S., Davis, A., 1985. The May 18, 1980, eruption of Mount St. Helens: 1. melt composition and experimental phase equilibria.

 J. Geophys. Res. 90, 2929.
- Scaillet, B., Clemente, B., Evans, B.W., Pichavant, M., 1998. Redox control of sulfur degassing in silicic magmas. J. Geophys. Res. 103, 23937–23949.
- Schneider, C.A., Rasband, W.S., Eliceiri, K.W., 2012. NIH image to ImageJ: 25 years of image analysis. Nat. Methods 9, 671–675.
- Scott, J.A.J., Mather, T.A., Pyle, D.M., Rose, W.I., Chigna, G., 2012. The magmatic plumbing system beneath Santiaguito Volcano, Guatemala. J. Volcanol. Geotherm. Res. 237–238, 54–68.
- Sparks, R.S.J., Marshall, L.A., 1986. Thermal and mechanical constraints on mixing between mafic and silicic magmas. J. Volcanol. Geotherm. Res. 29, 99–124.
- Streck, M.J., 2008. Mineral textures and zoning as evidence for open system processes. Rev. Mineral. Geochem. 69, 595–622.
- Sun, C., Lee, C.-T.A., 2022. Redox evolution of crystallizing magmas with C-H-O-S volatiles and its implications for atmospheric oxygenation. Geochim. Cosmochim. Acta 338, 302–321.
- Tepley, F.J., Davidson, J.P., Tilling, R.I., Arth, J.G., 2000. Magma mixing, recharge and eruption histories recorded in plagioclase phenocrysts from El Chichon Volcano, Mexico. J. Petrol. 41, 1397–1411.
- Tollan, P., Hermann, J., 2019. Arc magmas oxidised by water dissociation and hydrogen incorporation in orthopyroxene. Nat. Geosci. 12, 667–671.
- Toplis, M.J., Carroll, M.R., 1995. An experimental study of the influence of oxygen fugacity on Fe-ti oxide stability, phase relations, and mineral-melt equilibria in ferro-basaltic systems. J. Petrol. 36, 1137–1170.
- Venezky, D.Y., Rutherford, M.J., 1999. Petrology and Fe-Ti oxide reequilibration of the 1991 Mount Unzen mixed magma. J. Volcanol. Geotherm. Res. 89, 213–230.
- Wallace, P.A., Kendrick, J.E., Miwa, T., Ashworth, J.D., Coats, R., Utley, J.E.P., et al., 2019. Petrological architecture of a magmatic shear zone: a multidisciplinary investigation of strain localisation during magma ascent at Unzen volcano, Japan. J. Petrol. 60, 791–826.
- Wallace, P.J., 2005. Volatiles in subduction zone magmas: concentrations and fluxes based on melt inclusion and volcanic gas data. J. Volcanol. Geotherm. Res. 140, 217–240.
- Werner, C., Kelly, P.J., Doukas, M., Lopez, T., Pfeffer, M., McGimsey, R., Neal, C., 2013. Degassing of CO2, SO2, and H2S associated with the 2009 eruption of Redoubt Volcano, Alaska. J. Volcanol. Geotherm. Res. 259, 270–284.